



Title	STM/STS and SP-STS study of surface structural and electronic properties of Fe <sub>3</sub> O <sub>4</sub> (001) thin films
Author(s)	池内, 昭朗
Citation	北海道大学. 博士(工学) 甲第11752号
Issue Date	2015-03-25
DOI	10.14943/doctoral.k11752
Doc URL	<a href="http://hdl.handle.net/2115/58796">http://hdl.handle.net/2115/58796</a>
Type	theses (doctoral)
File Information	Akira_Ikeuchi.pdf



[Instructions for use](#)

# STM/STS and SP-STS study of surface structural and electronic properties of $\text{Fe}_3\text{O}_4(001)$ thin films

A Thesis

Submitted to The Graduate School of Information Science and Technology  
and The Committee on Graduate Studies  
of Hokkaido University  
In Partial Fulfillment of the Requirements  
for the Degree of Doctor of Philosophy

By

Akira Ikeuchi

March 2015

Nanoelectronics Laboratory  
Graduate School of Information Science and Technology  
Hokkaido University  
Sapporo, JAPAN

©Copyright2015 by AKIRA IKEUCHI  
All Rights Reserved

I certify that I have read this dissertation and that in my opinion it is fully adequate, in scope and quality, as a dissertation for the degree of Doctor of Philosophy.

Prof. K. Sueoka (Principal adviser)

---

Associate Prof. T. Koga

---

Prof. M. Yamamoto

---

Prof. A. Murayama

---

Approved by the University Committee on Graduate Studies

# Acknowledgements

First and foremost, I would like to express my gratitude to my family for always being supportive and never overbearing through all my time in graduate school. At this place, I would like to thank everybody who helped and supported me during the time I worked on this thesis. A few prominent ones are named for their special role.

I would like to express my best thank to my supervisor, Professor Kazuhisa Sueoka for his kind support and constant guidance throughout this work. He always treated me gently and gave me valuable advises.

I would like to express my appreciation to Associate Professor Takaaki Koga and Dr. Eiji Hatta for all valuable advises and discussions.

I would like to appreciate Professor Masafumi Yamamoto, Professor Akihiro Murayama and Associate Professor Takaaki Koga for reviewing my doctoral thesis.

I would like to express my deep appreciation to Dr. Agus Subagyo, who taught me fundamental parts of experiments and how to carry on a research work. Whenever I asked him something, he friendly gave me valuable advises, and whenever I consult about my life, he seriously gave me inspirational advises. I also would like to thank deeply Dr. Nobuyuki Ishida for his support when I was doing experiments in the Nanoelectronics lab when I started my first contact with STM and also my first lab life.

I would like to thank Mr. Satoshi Hiura for all valuable advises and discussions. He is extremely talented, so I was encouraged by him every time. I am honored to

be able to work with him.

I would like to thank Mr. Atsushi Sawada for all valuable advises and discussions. He is also talented person, and I was encouraged by him when I felt low. I have gone out drinking with him. That became a very good memory to me.

I would like to express my appreciation to Dr. Hirotaka Hosoi for all valuable advises and discussions.

I would like to be grateful to Ms. Michiyo Kanoh for her constant care about me and support concerning office procedures.

I would like to thank all members of Nanoelectronics laboratory for giving me a wonderful environment for continuing research work. The conversation, drinking parties and marathons with them made my life enjoyable through my PhD course.

Finally I would like to be most grateful to my parents Toshiaki and Namiko, Ikeuchi, and my wife Miku Ikeuchi. I am sure that I couldn't finish my PhD course without their constant care and tremendous supports.

# Table of Contents

Acknowledgements	ii
Table of Contents	iv
List of Figures	vii
<b>Part Introduction</b>	<b>1</b>
<b>Chapter 1 Theoretical Treatment of Scanning Tunneling Microscopy and Spectroscopy</b>	<b>6</b>
1.1 Scanning Tunneling Microscopy . . . . .	6
1.1.1 Tunneling effect . . . . .	7
1.1.2 Tunneling in STM configuration . . . . .	11
1.2 Scanning Tunneling Spectroscopy . . . . .	14
<b>Part I Fabrication and evaluation of spin-polarized tip for SP-STs measurement</b>	<b>16</b>
<b>Chapter 2 Introduction</b>	<b>19</b>
<b>Chapter 3 Experimental</b>	<b>20</b>
3.1 Ultra high vacuum system . . . . .	20
3.1.1 Preparation Chamber . . . . .	20
3.1.2 Analysis Chamber . . . . .	21
3.2 Fabrication of spin-polarized tip . . . . .	21

3.2.1	Modification of normal Omicron tip holder for VT-STM . . . . .	22
3.3	Electron Bombardment (EB) heating treatment . . . . .	23
3.4	Deposition of Fe . . . . .	25
3.5	Post annealing . . . . .	25
3.6	Standard specimen: Cr(001) single crystal . . . . .	26
3.7	Cleaning method of the standard specimen: Cr(001) single crystal cleaning . . . . .	26
<b>Chapter 4</b>	<b>Results and Discussion</b>	<b>28</b>
4.1	Cr(001) single crystal cleaning . . . . .	28
4.2	SP-STs measurements of Cr(001) by Fe/W tip . . . . .	34
 <b>Part II Surface atomic configurations around antiphase domain boundaries in Fe<sub>3</sub>O<sub>4</sub> films on MgO(001)</b>		 <b>36</b>
<b>Chapter 5</b>	<b>Introduction</b>	<b>39</b>
5.1	Crystal structure and Surface reconstruction of Fe <sub>3</sub> O <sub>4</sub> . . . . .	40
5.2	Antiphase domain boundary (APB) . . . . .	40
5.2.1	Formation of the APBs in Fe <sub>3</sub> O <sub>4</sub> films on MgO(001) . . . . .	40
5.2.2	Atomic structures around APBs on the Fe <sub>3</sub> O <sub>4</sub> (001) films surface	42
5.2.3	Magnetic coupling in Fe <sub>3</sub> O <sub>4</sub> films . . . . .	49
<b>Chapter 6</b>	<b>Experimental</b>	<b>53</b>
<b>Chapter 7</b>	<b>Results and Discussion</b>	<b>55</b>
7.1	STM measurements of the surface atomic structure on Fe <sub>3</sub> O <sub>4</sub> films surface . . . . .	55
7.2	STM measurements of the surface atomic structure around the APBs	55
7.2.1	in-plane 1/4[110] shift . . . . .	57
7.2.2	in-plane 1/2[100] shift . . . . .	59
7.2.3	out-of-plane 1/4[101] shift . . . . .	59
7.3	Observation of spin-polarized surface states on a Fe <sub>3</sub> O <sub>4</sub> film by SP-STs	65

<b>Chapter 8</b>	<b>Summary</b>	<b>69</b>
<b>Part III</b>	<b>Surface and subsurface electronic structures in <math>\text{Fe}_3\text{O}_4</math> films on <math>\text{MgO}(001)</math></b>	<b>70</b>
<b>Chapter 9</b>	<b>Introduction</b>	<b>73</b>
<b>Chapter 10</b>	<b>Experimental</b>	<b>76</b>
<b>Chapter 11</b>	<b>Results and Discussion</b>	<b>77</b>
11.1	Subsurface charge ordering . . . . .	77
<b>Chapter 12</b>	<b>Summary</b>	<b>83</b>
<b>References</b>		<b>84</b>
<b>Publication List</b>		<b>96</b>
<b>International Conference</b>		<b>97</b>

# List of Figures

Figure 1.1	Schematic of a one-dimensional potential barrier. . . . .	7
Figure 1.2	Schematic of a one-dimensional potential barrier. . . . .	8
Figure 1.3	Schematic of a one-dimensional potential barrier. . . . .	9
Figure 1.4	Schematic of a s wave tip model proposed by Tersoff and Hamann [1, 2]. The tip has a spherical end with a radius of curvature of $R$ . The center of the curvature is located at $r_0$ . The distance between the tip end and surface is $d$ . . . . .	13
Figure 3.1	UHV surface science system (Omicron Ltd.) . . . . .	21
Figure 3.2	Fabrication process of spin-polarized tip . . . . .	22
Figure 3.3	(a)Omicron official tip holder for VT-STM, (b)Modified tip holder for VT-STM . . . . .	23
Figure 3.4	Circuit diagram for EB heating . . . . .	24
Figure 3.5	(a) Mounting position of a tip, (b) Positional relationship between tip and filament. . . . .	24
Figure 3.6	SEM images of the tip. (a) Before EB heating, (b) After EB heating	25
Figure 3.7	Tunneling conductance vs sample voltage measurements of the Cr(001) surface obtained at constant height above the Fe surface.(after	

figure 5 in Ref. [3]) . . . . .	27
Figure 4.1 (a) STM image of Cr(001) single crystal surface ( $I_t = 0.3$ nA, $V_s = 0.8$ V), (b) $dI/dV$ curve taken at the terrace. . . . .	30
Figure 4.2 (a) STM image of Cr(001) single crystal surface ( $I_t = 0.3$ nA, $V_s = 0.2$ V), (b) $dI/dV$ curve taken at the terrace. . . . .	31
Figure 4.3 (a) STM image of Cr(001) single crystal surface ( $I_t = 0.3$ nA, $V_s = -0.12$ V), (b) $dI/dV$ curve taken at the terrace. . . . .	32
Figure 4.4 (a) STM image of Cr(001) single crystal surface ( $I_t = 0.3$ nA, $V_s = -0.1$ V), (b) $dI/dV$ curve taken at the terrace. . . . .	33
Figure 4.5 Results of SP-STs measurement on Cr(001) single crystal surface with Fe coted W tip at a tunneling current of 360 pA and a bias voltage of -170 mV. (a) Topographic image of Cr(001) single crystal surface. (b) $dI/dV$ map at a bias voltage of -170 mV for the same region shown in (a). (c) Line profiles of the topography and the $dI/dV$ signal taken along the white rectangle in (a) and black rectangle in (b). The relative position of the rectangles is same. . . . .	35
Figure 5.1 (a) Cubic inverse spinel structure of $\text{Fe}_3\text{O}_4$ . Tetrahedral iron ( $\text{Fe}_A$ ) in the A-plane, octahedral iron ( $\text{Fe}_B$ ) in the B-plane, and oxygen are indicated by a reddish circle, a bluish circle, and a grayish circle, respectively. (b) Four possible types of surface unit cells in unrelaxed B-plane termination $\text{Fe}_3\text{O}_4(001)$ surfaces. Precise surface relaxation should be considered, and surface unit cells do not coincide with the actual unit cell on the surfaces. However, it is convenient to use these unit cells for understanding atomic arrangements around APBs. . . . .	41
Figure 5.2 First monolayer of $\text{Fe}_3\text{O}_4$ on MgO(001) substrate. . . . .	42

- Figure 5.3 Atomic structure models near the APB with  $1/4[110]$  shift vector. (a) shows the first oxygen layer with octahedral sites and the tetrahedral sites directly below this plane and (b), (c) and (d) show the second third and fourth layer respectively. . . . . 45
- Figure 5.4 Atomic structure models near the APB with  $1/2[100]$  shift vector. (a) shows the first oxygen layer with octahedral sites and the tetrahedral sites directly below this plane and (b), (c) and (d) show the second third and fourth layer respectively. . . . . 46
- Figure 5.5 Atomic structure models near the APB with  $1/4[101]$  shift vector and (010) boundary plane. (a) shows the first oxygen layer with octahedral sites and the tetrahedral sites directly below this plane and (b), (c) and (d) show the second third and fourth layer respectively. 47
- Figure 5.6 Atomic structure models near the APB with  $1/4[101]$  shift vector and (130) boundary plane. (a) shows the first oxygen layer with octahedral sites and the tetrahedral sites directly below this plane and (b), (c) and (d) show the second third and fourth layer respectively. 48
- Figure 5.7 Atomic structure models of ideal bulk  $\text{Fe}_3\text{O}_4$ . (a) and (b) show the first oxygen layer with octahedral sites and the tetrahedral sites directly below this plane. Examples of magnetic couplings are indicated as green lines. The directions of the spin are indicated as black arrows. . . . . 50
- Figure 5.8 Atomic structure models near the APB with  $1/4[101]$  shift vector and (010) boundary plane. Figure shows the first oxygen layer with octahedral sites and the tetrahedral sites directly below this plane. Examples of magnetic superexchange interactions across the boundary are indicated as green lines. . . . . 52
- Figure 7.1 (a) STM image of  $\text{Fe}_3\text{O}_4$  film on  $\text{MgO}(001)$ . The feedback control

- set point was  $V_S = 2.0$  V,  $I = 1$  nA. The scan size was  $50 \times 50$  nm<sup>2</sup>. Atomically flat terraces exhibiting atomic rows oriented along the [110] direction can be seen. (b) Line profile taken along the black line in the STM image. The step height of  $\sim 0.21$  nm is indicated. 56
- Figure 7.2 High-resolution STM image of Fe<sub>3</sub>O<sub>4</sub> film on MgO(001). The feedback control set point was  $V_S = 2.0$  V,  $I = 1$  nA. The scan width was 5 nm. The  $(\sqrt{2} \times \sqrt{2})R45^\circ$  reconstruction unit cell is indicated by the yellow square. . . . . 56
- Figure 7.3 (a) STM image of an APB with a  $1/4[110]$  shift. The feedback control set point was  $V_S = 2.0$  V,  $I = 0.3$  nA. The scan size was  $5 \times 5$  nm<sup>2</sup>. The APB is in a (110) plane. (b) Possible surface atomic configuration around an APB with a  $1/4[110]$  shift. . . . . 60
- Figure 7.4 (a) STM image of an APB which has a  $1/4[110]$  shift. The feedback control set point was  $V_S = 1.5$  V,  $I = 0.7$  nA. The scan size was  $5 \times 5$  nm<sup>2</sup>. (b) Possible surface atomic configuration around an APB with a  $1/4[110]$  shift. . . . . 61
- Figure 7.5 (a) STM image of an APB with a  $1/4[110]$  shift. The feedback control set point was  $V_S = 1.5$  V,  $I = 0.8$  nA. The scan size was  $5 \times 5$  nm<sup>2</sup>. (b) and (c) Possible surface atomic configuration around an APB with a  $1/4[110]$  shift. . . . . 62
- Figure 7.6 (a) STM image of an APB with a  $1/2[100]$  shift. The feedback control set point was  $V_S = 1.6$  V,  $I = 1$  nA. The scan size was  $5 \times 5$  nm<sup>2</sup>. The APB is in a (100) plane. (b) Possible surface atomic configuration around an APB with a  $1/2[100]$  shift. . . . . 63
- Figure 7.7 (a) STM image of an APB with a  $1/4[101]$  shift. The feedback control set point was  $V_S = 2.0$  V,  $I = 1$  nA. The scan size was  $5 \times 5$  nm<sup>2</sup>. The APB is in a (100) plane. (b) Possible surface atomic configu-

- ration around an APB with a  $1/4[101]$  shift and a (110) boundary plane. (c) STM image of an APB with a  $1/4[101]$  shift. The feedback control set point was  $V_S = 2.0$  V,  $I = 0.3$  nA. The scan size was  $5 \times 5$  nm<sup>2</sup>. The APB is in a ( $\bar{1}30$ ) plane. (d) Possible surface atomic configuration around an APB with a  $1/4[101]$  shift and a ( $\bar{1}30$ ) boundary plane. . . . . 64
- Figure 7.8 (a)  $(10 \times 10)$  nm<sup>2</sup> STM image of the topography. The image of the Fe<sub>3</sub>O<sub>4</sub>(001) film was taken with Cr/W-tip at a tunneling current of 0.3 nA and a bias voltage of 1.2 V. (b)  $dI/dV$  map at a bias voltage of 1.2 V for the same region shown in (a). (c) Histograms of  $dI/dV$  signal intensity derived from the area indicated by black solid rectangles in Fig. 7.8(b). (d) Histograms of  $dI/dV$  signal intensity derived from the area indicated by black dashed rectangles in Fig. 7.8(b) . . . . 67
- Figure 7.9 a)  $(10 \times 10)$  nm<sup>2</sup> STM image of the topography. The image of the Fe<sub>3</sub>O<sub>4</sub>(001) film was taken with Cr/W-tip at a tunneling current of 0.3 nA and a bias voltage of 1.2 V. (b)  $dI/dV$  map at a bias voltage of 1.2 V for the same region shown in (a). (c) Histograms of  $dI/dV$  signal intensity derived from the area indicated by black solid rectangles in Fig. 7.9(b). (d) Histograms of  $dI/dV$  signal intensity derived from the area indicated by black dashed rectangles in Fig. 7.9(b) . . . . 68
- Figure 9.1 (a) Model of the B-terminated surface structure of Fe<sub>3</sub>O<sub>4</sub>(001) proposed by Pentcheva et al [4–6]. The black arrows indicate the directions of the displacements of octahedral irons. The narrow and wide section are marked as “n” and “w”. (b) Model of the subsurface charge ordering structure with a  $(\sqrt{2} \times \sqrt{2})R45^\circ$  reconstructed unit cell. The  $(\sqrt{2} \times \sqrt{2})R45^\circ$  cell is indicated by a black square. . . . 75
- Figure 11.1 (a)  $(2.5 \times 2.5)$  nm<sup>2</sup> STM image of the Fe<sub>3</sub>O<sub>4</sub>(001) film. The image was taken with Cr/W-tip at a tunneling current of 0.3 nA and a

bias voltage of 1.2 V. The  $(\sqrt{2} \times \sqrt{2})R45^\circ$  reconstruction unit cell is indicated by the white square. The narrow and wide section are marked as “n” and “w”. Individual  $\text{Fe}_B$  ions are imaged. (b) Line profiles taken along  $[1\bar{1}0]$  and  $[110]$  directions marked as “A” and “B” in (a). . . . . 78

Figure 11.2 (a)  $(4.7 \times 4.7)$  nm<sup>2</sup> STM image of the topography. The image of the  $\text{Fe}_3\text{O}_4(001)$  film was taken with Cr/W-tip at a tunneling current of 0.3 nA and a bias voltage of 1.2 V. The dashed line indicates an APB. (b)  $dI/dV$  map at a bias voltage of 1.2 V for the same region shown in (a). The white open rectangle indicates the  $(\sqrt{2} \times \sqrt{2})R45^\circ$  reconstruction unit cell. The narrow and wide section are marked as “n” and “w”. (c) Line profiles of the topography and the  $dI/dV$  signal taken along the arrows marked as “C” and “D” in (a) and (b), respectively. The relative position of the arrows is same. . . . . 80

Figure 11.3 (a) Top and (b) side views of the  $\text{Fe}_3\text{O}_4(001)$  surface. Panel (b) only shows the 3 outermost planes, indicating the different in-plane  $\text{Fe}_B$ - $\text{Fe}_B$  distance in Å. (c) Spin-resolved DOS of all inequivalent atoms (blue for Fe, red/green for surface O) at the outermost B-plane. [7] 81

Figure 11.4 (a)  $(3 \times 3)$  nm<sup>2</sup> STM image of the  $\text{Fe}_3\text{O}_4(001)$  film. The image was taken with Cr/W-tip at a tunneling current of 0.2 nA and a bias voltage of 1.2 V. The locations of STM tip for STS measurements are indicated by red circle( $\circ$ ), blue cross( $\times$ ), green triangle ( $\triangle$ ) and black cross( $+$ ). (b)  $(dI/dV)/(\overline{I/V})$  curves taken on surface  $\text{Fe}_B$  sites. These curves were taken at the corresponding mark and converted from the  $I(V)$  curve using the procedure developed by Feenstra *et al.* [8] . . . . . 82

**Part**

**Introduction**



# Introduction

Magnetite ( $\text{Fe}_3\text{O}_4$ ) is a magnetic iron oxide that has the unique properties such as half-metallicity, high Curie temperature of 858 K and metal-insulator (Verwey) transition at 120 K in a bulk [9–11]. Moreover,  $\text{Fe}_3\text{O}_4$  is abundantly present in the earth and harmless to the human body. In the past decades,  $\text{Fe}_3\text{O}_4$  has been drawing intense research interest because of their potential applications in magnetic devices, spintronic devices, catalyst, drug delivery, and electrodes. Due to these superior properties, it is highly desirable to  $\text{Fe}_3\text{O}_4$  into thin film form. The fabrication of high quality  $\text{Fe}_3\text{O}_4$  thin films has been attempted by several deposition methods such as molecular beam epitaxy [12–17], sputtering [18], and pulsed laser deposition [19, 20]. Many groups have succeeded in depositing  $\text{Fe}_3\text{O}_4$  on various substrates (MgO, SrTiO<sub>3</sub>, MgAl<sub>2</sub>O<sub>4</sub>, sapphire, and Si) [14, 19, 21–23]. However, these thin films show decreased electrical conductivity [14], unsaturated magnetization [18, 24], and low magnetoresistance [25, 26]. It has been also reported that ultrathin films below 5 nm become superparamagnetic [21]. Epitaxially grown  $\text{Fe}_3\text{O}_4$  films are well known to contain a high density of antiphase domain boundaries (APBs) as investigated by transmission electron microscopy (TEM) [14, 18]. It is believed that these anomalous properties are a result of the presence of the APBs and the existence of a strong antiferromagnetic coupling across the APBs. K. P. McKenna *et al.* have recently demonstrated that APB defects on the  $\{110\}$  planes are unusually stable and induce antiferromagnetic coupling between adjacent domains by high-resolution TEM and theoretical calculation [27]. The literature concerning the atomic configuration and magnetic coupling of APB defect on the  $\{100\}$  and  $\{130\}$  is, however, limited. It is needed that the investigation of the atomic configuration of the APBs with atomic

---

resolution.

At the surface of  $\text{Fe}_3\text{O}_4(001)$ , the disappearance of the half-metallicity and the emergence of a surface verwey transition at room temperature have been reported [5, 28]. Because of these properties and phenomena,  $\text{Fe}_3\text{O}_4$  is a fascinating material for the understanding of the electronic correlation effects in oxides. It is well known that the  $(\sqrt{2} \times \sqrt{2})R45^\circ$  reconstruction pattern is observed by low energy electron diffraction (LEED) measurement of  $\text{Fe}_3\text{O}_4(001)$  surface [29, 30]. Up to date, a significant number of attempts has been under taken to understand the atomic structure of  $\text{Fe}_3\text{O}_4(001)$  surface (i.e. the origin of the  $(\sqrt{2} \times \sqrt{2})R45^\circ$  reconstruction) [4–6, 31–36]. Scanning tunneling microscopy (STM) measurements have observed several types of surface reconstruction, and revealed that the surface atomic arrangement is highly dependent on the sample preparation procedure. S. A. Chambers *et al.* have reported an A-terminated surface contains Fe cation on tetrahedral A site by STM [31]. On the other hand, a B-terminated surface contains Fe cation on octahedral B site has been also observed by STM [12, 13, 32, 33, 37–40]. Emergence of the B-terminated surface structure has been also predicted by theoretical calculations performed by Pentcheva *et al.* [4, 6]. They suggested that the  $(\sqrt{2} \times \sqrt{2})R45^\circ$  reconstruction is a result of a Jahn-Teller distortion and that the reconstructed B-terminated surface is the most stable energetically compare to the A-terminated and non reconstruct surface [4]. However, the origin of the  $(\sqrt{2} \times \sqrt{2})R45^\circ$  reconstruction still remains under discussion. The investigation of the surface structural and electronic properties of  $\text{Fe}_3\text{O}_4$  at the atomic scale is necessary for future oxide based device development.

Among many apparatus used for the investigation of surfaces/interfaces, for example, auger electron spectroscopy (AES), low energy electron diffraction (LEED), photoemission spectroscopy (PES), electron energy loss spectroscopy (EELS) and so on, scanning tunneling microscopy (STM) is one of the most powerful tools that provide the geometric information at surface. The STM also makes it possible to perform the local tunneling spectroscopy called scanning tunneling spectroscopy (STS), which provides the variety of spectroscopic information, such as local density of states (LDOS) [41, 42], elementary excitation of phonon, magnon [43] and

---

plasmon, etc. These two features of STM/STS, i.e., high resolved imaging of surface geometry and local tunneling spectroscopy, allow us to correlate the structural and electronic properties at surface with unprecedented spatial resolution [44]. For that reasons, STM/STS have been widely used for the investigation of the defects, adsorbed atoms [45, 46] and any local phenomena at the surfaces. Recently, spin-polarized scanning tunneling microscopy (SP-STM) [47, 48] and spin-polarized scanning tunneling spectroscopy [49, 50] (SP-STs) that have a sensitivity for spin of tunneling electron are used for the investigation of surface magnetism.

In this work, we have performed STM and STS on  $\text{Fe}_3\text{O}_4(001)$  films using a nonmagnetic W tip and a magnetic film coated tip, in order to reveal surface atomic and electronic structure on the  $\text{Fe}_3\text{O}_4(001)$  films include the APBs. The atomic structure of the APBs and its effects on the electronic structure near the APBs are investigated.

# Chapter 1

## Theoretical Treatment of Scanning Tunneling Microscopy and Spectroscopy

### 1.1 Scanning Tunneling Microscopy

Scanning tunneling microscopy (STM) was invented by G. Binnig and H. Rohrer in 1982 [51, 52] as a novel type of microscopy that had unprecedented high spatial resolution down to the atomic scale [44].

Thanks to the inventors, G. Binnig and H. Rohrer, we have been able to access to the atomic world since then. Instead of using a lens as conventional microscopes, the STM uses sharpened conducting material named as tip to image the geometric and electronic structures of surface of conducting material. The tip is attached to a piezoelectric actuator that can control the tip position with high precision. During the measurement bias voltage is applied between the tip and sample, and the tip is brought closer to the sample surface until the tunneling current begins to flow. The typical tip-sample distance is less than 1 nm. With keeping the tunneling current constant, the tip is scanned over the sample surface. The trajectory of the tip, i.e., motion of the piezoelectric actuator is imaged as a topographic image. Although the implementation of STM is not so easy task, the principle of operation is very simple and it is easy to understand intuitively. The key mechanism is based on the fundamental quantum effect, "tunneling".

### 1.1.1 Tunneling effect

In classical mechanics, a ball with potential energy ( $U$ ) is described by

$$\underbrace{\frac{p^2}{2m}}_{\text{kinetic energy}} + \underbrace{U}_{\text{potential energy}} = \underbrace{E}_{\text{total energy}}, \quad (1.1)$$

where  $m$  is the mass of the ball and  $E$  is the total energy. The momentum of the ball  $p = [2m(E - U)]^{1/2}$ . When  $p > 0$ , the ball is moving. Considering the case of an electron in a potential  $U(z)$ , the electron is described by

$$\frac{p^2}{2m} + U(z) = E, \quad (1.2)$$

where  $m$  is the electron mass and  $E$  is the energy. The potential is expressed as follows (Fig.1.1)

$$U(z) = \begin{cases} 0 & z < 0 \\ U_0 & 0 \leq z \leq a \\ 0 & z > a \end{cases}. \quad (1.3)$$

In the region,  $E > U(z)$ , the electron has non-zero momentum  $p = [2m(E - U)]^{1/2}$

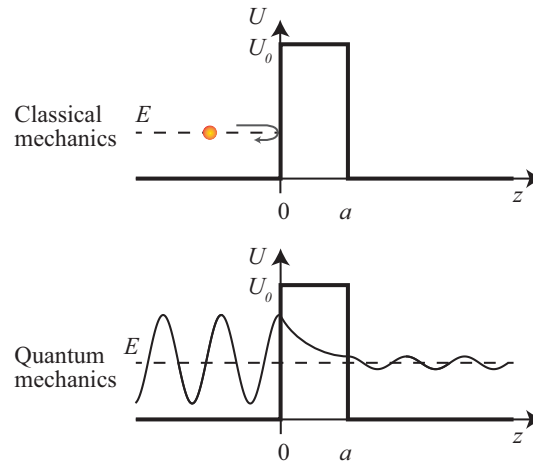


**Figure 1.1** Schematic of a one-dimensional potential barrier.

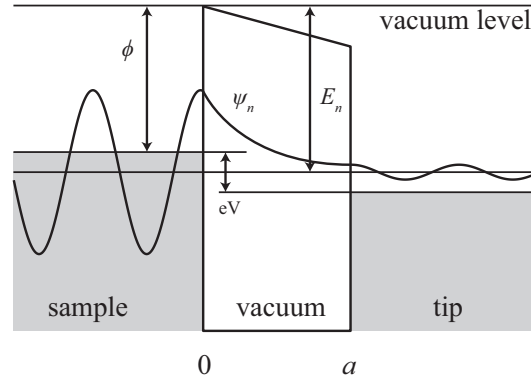


**Figure 1.2 Schematic of a one-dimensional potential barrier.**

as same as the case of the ball. On the other hand, the electron cannot have momentum in the region  $E < U_0$ . Therefore, in the classical mechanics, the electron cannot pass through a potential barrier. In quantum mechanics, any particle such as the electron has wave-like characteristics. The electrons can penetrate (tunnel) through the potential barrier in the case of  $a$  is very short distance up to a few Angstroms (see Fig.1.1). Here we think a one-dimensional metal-vacuum-metal tunneling junction as shown in Fig.1.2. The state of the electron is described by a wavefunction  $\psi(z)$ . The one-dimensional Schrödinger equation for the electron is expressed as

$$-\frac{\hbar^2}{2m} \frac{d^2\psi(z)}{dz^2} + U(z)\psi(z) = E\psi(z), \quad (1.4)$$

where the  $\hbar$  is the Plank's constant divided by  $2\pi$ ,  $m$  is a mass of the particle,  $\psi(z)$  is the wave function of the electron,  $U(z)$  is the potential energy and  $E$  is the total energy of the electron. In the region,  $0 < z < a$ , Eq. (1.4) has solution

$$\psi(z) = \psi(0)e^{-\kappa z}. \quad (1.5)$$

It is decaying with the decay constant

$$\kappa = \frac{\sqrt{2m\phi}}{\hbar} \quad (1.6)$$

where  $\phi$  is the barrier height. It can be roughly approximated as

$$\phi = \frac{\phi_S + \phi_T}{2} \quad (1.7)$$

where  $\phi_S(\phi_T)$  is the work function of the sample(tip), and we assume that  $\phi_S$  and  $\phi_T$  are equal in order to simplify discussion. The probability of the electron tunneling through the vacuum gap of width  $a$  is proportional to

$$|\psi(a)|^2 = |\psi(0)|^2 e^{-2\kappa a}, \quad (1.8)$$

which has a non-zero value. Therefore it has a non-zero probability of tunneling through the vacuum gap which has small  $a$ .

The easiest way to understand the principle of STM operation is to solve the one-dimensional time-independent Schrödinger equation for square potential barrier. The problem is introduced in most textbooks of quantum mechanics.

Consider the motion of a particle having energy  $E$  in the potential expressed as follows (Fig. 1.3).

$$V(x) = \begin{cases} 0 & z < 0 \\ V_0 & 0 \leq z \leq a \\ 0 & z > a \end{cases} \quad (1.9)$$

If the particle proceeds to the potential barrier from the left side, according to the

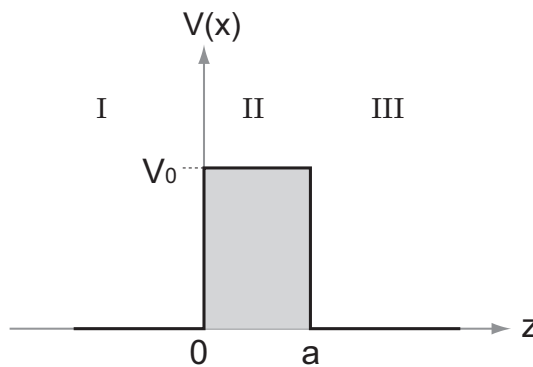


**Figure 1.3 Schematic of a one-dimensional potential barrier.**

classical mechanics, the particle will be reflected at  $z = 0$  and never proceed to the right side of the potential barrier. On the other hand, for a small particle like electron, we should apply quantum mechanics to investigate the motion, which results in the totally different picture due to the wave-particle dualism. The incoming

particle to the potential barrier has a certain probability to exist even in the region  $E < V$  and penetrate the potential barrier with a certain probability. Then, the particle proceeds to the right side of the barrier ( $z > a$ ) as explained below.

The one-dimensional Schrödinger equation for a particle is expressed as

$$\frac{-\hbar^2}{2m} \frac{d^2\psi(z)}{dz^2} + V(z)\psi(z) = E\psi(z), \quad (1.10)$$

where the  $\hbar$  is the Plank's constant divided by  $2\pi$ ,  $m$  is a mass of the particle,  $\psi(z)$  is the wave function of the particle,  $V(z)$  is the potential energy and  $E$  is the total energy of the particle. At first, we consider three region independently: region I, left of the barrier ( $z < 0$ ), region II, barrier region ( $0 < z < a$ ), and region III, right of the barrier ( $z > a$ ). Then the respective wave function will be matched using the boundary condition. For region I and III the Schrödinger equation is given by

$$\frac{d^2\psi(z)}{dz^2} = -\frac{\sqrt{2mE}}{\hbar^2}\psi(z). \quad (1.11)$$

The general solution of 1.11 becomes

$$\psi(z) = Ae^{ikz} + Be^{-ikz} \quad (z < 0), \quad (1.12)$$

$$\psi(z) = Ce^{ikz} + De^{-ikz} \quad (z > a), \quad (1.13)$$

$$k = \frac{\sqrt{2mE}}{\hbar}, \quad (1.14)$$

where A, B, C and D are arbitrary constants. For region II, the the Schrödinger equation is given by

$$\frac{d^2\psi(z)}{dz^2} = \frac{\sqrt{2m(E - V_0)}}{\hbar}\psi(z) \quad (1.15)$$

The general solution of 1.11 becomes

$$\psi(z) = Fe^{\kappa z} + Ge^{-\kappa z}, \quad (1.16)$$

$$\kappa = \frac{\sqrt{2m(E - V_0)}}{\hbar}, \quad (1.17)$$

where G and F are arbitrary constants. Note that we are now considering the solution for the particle coming from the left side of potential. Therefore, D should be

zero because no reflection will occur for  $z > a$ . Schrödinger equation requires the continuous  $\psi(z)$  and the first derivative  $\frac{d\psi(z)}{dz}$  for all  $z$ , namely,  $\psi_I(0) = \psi_{II}(0)$ ,  $\frac{d\psi_I}{dz}\Big|_{z=0} = \frac{d\psi_{II}}{dz}\Big|_{z=0}$ ,  $\psi_{II}(a) = \psi_{III}(a)$ ,  $\frac{d\psi_{II}}{dz}\Big|_{z=a} = \frac{d\psi_{III}}{dz}\Big|_{z=a}$ . As a result, the following condition has to be fulfilled.

$$A + B = F + G, \quad (1.18)$$

$$ik(A - B) = \kappa(F - G), \quad (1.19)$$

$$Fe^{\kappa a} + Ge^{-\kappa a} = Ce^{-i\kappa a}, \quad (1.20)$$

$$\kappa Fe^{\kappa a} - \kappa Ge^{-\kappa a} = ikCe^{i\kappa a}. \quad (1.21)$$

Solving this simultaneous equation, we can determine other coefficient of B, C, G and F in terms of A. A value of A can be determined from the normalization condition of the wave function. Using the obtained wave function, the probability flux can be calculated. The ratio of the incident probability flux and transmitted probability flux give the transmission coefficient  $T$  as

$$T = \frac{1}{1 + \frac{(k^2 + \kappa^2)}{4k^2\kappa^2 \sinh^2(\kappa a)}}. \quad (1.22)$$

When  $\kappa a \gg 1$  corresponding to the strongly attenuating barrier, the  $T$  is approximated as

$$T \approx 16 \frac{k^2 \kappa^2}{(k^2 + \kappa^2)^2} \exp(-2\kappa a). \quad (1.23)$$

The exponential dependence of  $T$  on the barrier width is the key factor for the STM operation, which makes it possible to detect the slight change of tip-sample separation through the tunneling current. Assuming the work function of sample is 4 eV, we get the value of decay constant  $\kappa = 1 \text{ \AA}^{-1}$ . As a result, if the tip-sample distance is changed by 1  $\text{\AA}$ , the tunneling current will be reduced by 86 % ( $1/e^2$ ).

### 1.1.2 Tunneling in STM configuration

In 1961, Bardeen developed time-dependent perturbation approach as a basic theory for tunneling junction [53]. The advantage of the Bardeen's approach compared to the time-independent one in previous section is that it is applicable to the

three-dimensional case. Therefore, his approach was further developed for the three dimensional tunneling junction in STM [1, 2, 54–56], which provided the insight into the physics in STM. In this section, I briefly introduce a theory of tunneling process in STM configuration in the Bardeen’s approach scheme developed by Tersoff and Hamann [1, 2].

Consider the STM configuration in which the bias voltage is applied to sample with respect to the tip. Using Bardeen’s approach, tunneling current  $I$  can be expressed as

$$I = \frac{2\pi e}{\hbar} \sum_{t,s} \{f(E_t)[1 - f(E_s + eV)] - f(E_s + eV)[1 - f(E_t)]\} |M_{ts}|^2 \delta(E_s - E_t), \quad (1.24)$$

where the  $f(E)$  is the Fermi-Dirac distribution function,  $V$  is the bias voltage,  $M_{ts}$  is the tunneling matrix element between tip ( $\psi_t$ ) and sample ( $\psi_s$ ) electronic states and  $E_t$  ( $E_s$ ) is the energy of states  $\psi_t$  ( $\psi_s$ ). The tunneling matrix element, according to Bardeen, can be given by

$$M_{ts} = \frac{-\hbar^2}{2m} \iint_S (\psi_t^* \nabla \psi_s - \psi_s \nabla \psi_t^*) d\mathbf{S}, \quad (1.25)$$

where the integration is carried out over a surface which is located entirely within the barrier region. To calculate the matrix element, the wave function of the tip and sample have to be known, however, it is almost impossible to extract the explicit expression for the tip states due to the lack of information of the atomic geometry of the tip apex. Tersoff and Hamann introduce the simplified model for a tip called s wave tip. They assume a probe tip that has spherical end with radius of curvature of  $R$  as shown in Fig. 1.4. The center of the curvature is located at  $r_0$ . The distance between the tip end and surface is  $d$ . In this model, wave function with s symmetry ( $l = 0$ ) is only considered, whereas wave functions having the angular momentum ( $l \neq 0$ ) are ignored. In the limit of low temperature and small bias voltage, Tersoff and Hamann calculated the tunneling current, which is proportional to

$$I \propto V \cdot n_t(E_F) \cdot \exp(2\kappa R) \cdot \sum_s |\psi_s(\mathbf{r}_0)|^2 \delta(E_s - E_F), \quad (1.26)$$

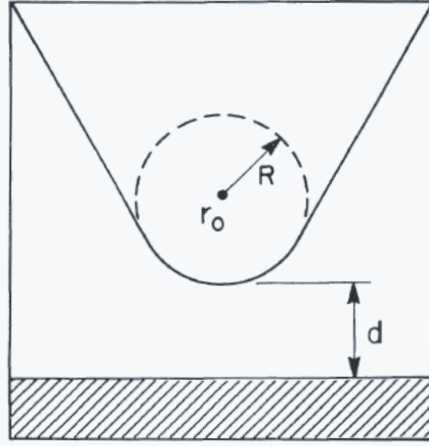


**Figure 1.4** Schematic of a s wave tip model proposed by Tersoff and Hamann [1, 2]. The tip has a spherical end with a radius of curvature of  $R$ . The center of the curvature is located at  $r_0$ . The distance between the tip end and surface is  $d$ .

where  $V$  is the bias voltage,  $n_t(E_F)$  is the density of states (DOS) of the tip at the Fermi energy and  $\kappa = \sqrt{(2m\phi)/\hbar}$  where  $\phi$  is the effective local potential barrier height. The quantity

$$n_s(E_F, \mathbf{r}_0) = \sum_s |\psi_s(\mathbf{r}_0)|^2 \delta(E_s - E_F) \quad (1.27)$$

is the local density of states (LDOS) of the sample at the Fermi energy evaluated at the center of the s wave tip. Eq. (1.26) indicates that in the limitation of low temperature and low bias voltage, STM image in a constant tunneling current mode shows the contour of the constant surface LDOS at the Fermi energy evaluated at the center of the s wave tip.

The generalization of Eq. (1.26) to the finite bias voltage is too complicated, because finite bias voltage distort the tip and sample wave function as well as the energy eigenvalues. However, if we take zero-voltage wave functions and energy eigenvalue as a first order approximation, the effect of the bias voltage is just the shift of sample wave function and eigenvalue with respect to those of the tip in

energy. Then, the Eq. (1.26) can be generalized as

$$I \propto \int_0^{eV} n_t(E - eV) \cdot n_s(E, \mathbf{r}_0) dE, \quad (1.28)$$

where  $n_t(E)$  is the DOS for the tip,  $n_s(E, \mathbf{r}_0)$  is the DOS for the sample evaluated at the center of s wave tip. The energy levels are evaluated with respect to the Fermi energy.

## 1.2 Scanning Tunneling Spectroscopy

In the previous section, the tunneling current evaluated in the Tersoff-Hamann scheme is introduced. In Eq. (1.28), the quantity  $n_s(E, \mathbf{r}_0)$  can be modified to

$$n_s(E, \mathbf{r}_0) = n_s(E) \cdot \exp\{-2\kappa(d + R)\}, \quad (1.29)$$

where  $n_s(E)$  is the LDOS evaluated at sample surface. Then, using the WKB approximation, the exponential decay component  $\exp\{-2\kappa(s + R)\}$ . is calculated as

$$\exp\{-2\kappa(d + R)\} = \exp\left\{-2(d + R) \left[ \frac{2m}{\hbar^2} \left( \frac{\phi_t + \phi_s}{2} + \frac{eV}{2} - E \right) \right]^{\frac{1}{2}}\right\}. \quad (1.30)$$

where  $\phi_t, \phi_s$  are the work function of tip and sample, respectively. As a consequence, we finally obtain the expression of tunneling current as

$$I \propto \int_0^{eV} n_t(E - eV) \cdot n_s(E) \cdot T(E, eV) dE, \quad (1.31)$$

where the  $T(E, eV)$  is the energy and bias dependent tunneling transmission probability function expressed as

$$\exp\left\{-2(d + R) \left[ \frac{2m}{\hbar^2} \left( \frac{\phi_t + \phi_s}{2} + \frac{eV}{2} - E \right) \right]^{\frac{1}{2}}\right\}. \quad (1.32)$$

Assuming the  $n_t$  is independent of  $E$ , the differentiation of tunneling current with respect to  $V$  becomes

$$\frac{dI}{dV} \propto n_t(0)n_s(eV)T(eV) + \int_0^{eV} n_t(E - eV)n_s(E) \frac{dT(E, eV)}{dV} dE. \quad (1.33)$$

As can be seen in the first term,  $dI/dV$  reflect the LDOS of the sample at the energy  $eV$  with respect to the Fermi level. Therefore, if we measure the  $dI/dV$  dependence on bias voltage  $V$ , we can extract the bias dependent LDOS structures. The second term work as the background variation due to the bias dependence of the transmission coefficient. Among several types of spectroscopy in STS,  $dI/dV$  is the most extensively measured spectrum to investigate the LDOS structure of sample surfaces. Especially surface states appeared as protrusion in  $dI/dV$  spectrum is often explored.

# Part I

## Fabrication and evaluation of spin-polarized tip for SP-STTS measurement



# Abstract

In this part, the SP-STM/STS experiments of Cr(001) will be summarized. We have studied surface magnetic domain on Cr(001) single crystal by SP-STM/STS with spin sensitive tip. The spin sensitive tips were fabricated by coating Fe, ferromagnetic material, on W tips which treated by electron bombardment (EB) heating. We have developed STM tip holders in order to be able to use for treatment the tips, such as EB heating and the coating magnetic materials. Scanning electron microscopy is used to characterize the radius of the tips apex before and after EB heating. The Cr(001) single crystal surface was cleaned with thermal heating and ion-sputtering. SP-STM/STS using Fe coated W tip is also performed on the Cr(001) single crystal in order to confirm the capability of the spin sensitivity of the Fe coated W tip.

# Chapter 2

## Introduction

Spintronics is an emerging field of electronics using electron spin different from conventional way using electron charge. Studies of new type spintronics devices such as quantum information device using spin states are advancing rapidly, and micro scale magnetics has recently received broad attention due to the miniaturization and high-density of the magnetic devices. These devices are using magnetic films, magnetic nanostructures and hybrid structures of magnetic material and semiconductor. Therefore, measurement and visualization of spin information of magnetic materials with atomic scale are highly significant. SP-STs has been drawing intense research interest because of its abilities such as imaging of surface topography and spin information with atomic scale [43, 57–65]. SP-STs is an application of the STM. In a STM/STs measurement, non magnetic tips (e.g. W tip) are commonly used. On the other hand, it is necessary that both of the tip apex and sample are spin-polarized for the SP-STs measurement. Especially, it is difficult to fabricate the spin-polarized tips. To date, several way of the spin-polarized tip fabrication have been proposed. In this study, We use the method coating a W tip with a magnetic film. In order to evaluate the spin-polarized tip, we conducted SP-STs measurements of Cr(001) surface.

# Chapter 3

## Experimental

### 3.1 Ultra high vacuum system

The STM, STS and SP-STS is operating in a ultra high vacuum (UHV) chamber shown in Fig.3.1. The UHV system is mainly composed of two chamber; an analysis chamber and a preparation chamber. Our STM/STS and SP-STS measurements were performed in Analysis chamber. This chamber is equipped with a commercial variable temperature STM (VT-STM) and UHV STM system (Omicron Ltd.), our experiments were mainly performed by VT-STM system. Vacuum in the UHV system is achieved by a combination of turbo molecular pumps (TMP), sputter ion pumps (SIP), and a titanium sublimation pump (TSP). The base pressure of both chambers was below  $2.0 \times 10^{-10}$  mbar. We will describe the details of two chamber below.

#### 3.1.1 Preparation Chamber

This chamber is for sample preparation, which is equipped with facilities for it such as evaporators (Omicron Ltd., Electron beam evaporator with flux monitor: EFM3), a sample and tip heating system, a ion sputter gun, and reflection high energy electron diffraction (RHEED) optics.

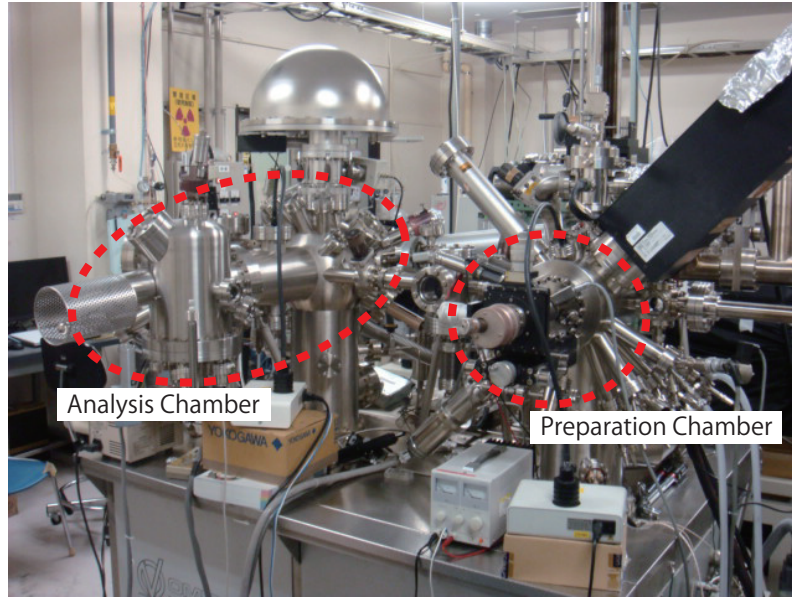


**Figure 3.1** UHV surface science system (Omicron Ltd.)

### 3.1.2 Analysis Chamber

This chamber is for sample preparation and characterization, which is equipped with facilities for those such as an evaporator (EFM3), a sample heating system, low energy electron diffraction (LEED) optics, X-ray photoelectron spectroscopy system, UHV-STM (Omicron Ltd.) system, and variable temperature STM (VT-STM) system.

## 3.2 Fabrication of spin-polarized tip

Several fabrication method for spin-polarized tip have been proposed such as using bulk magnetic material tips [13, 47], optically pumped GaAs tips [66–69], and magnetic materials covered W tips [49, 70–72]. In particular, W tips covered with magnetic materials are most commonly used for SP-STs measurements. In this study, we adopted the magnetic materials covered W tip. We choose the Fe as the ferromagnetic material in order to fabricate the in plane magnetized spin-polarized

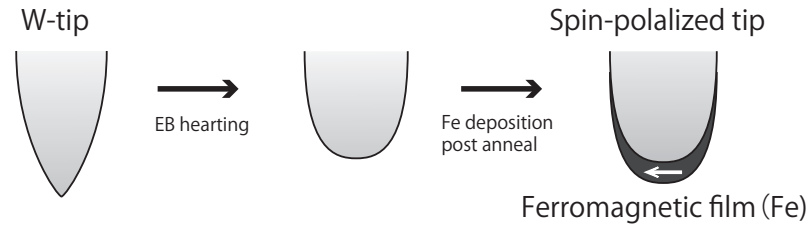


**Figure 3.2 Fabrication process of spin-polarized tip**

tip. First, a W-tip was heated up to 2200 K by electron bombardment (EB) heating method in order to clean the tip surface and make the curvature radius of the tip apex larger moderately. This larger curvature radius is needed for the following reason: If the tip is too sharp, the shape anisotropy is strong and then the magnetic moment of the tip apex is likely to be rotated out of plane of the sample. Then, we carried out a Fe deposition to the tip apex at room temperature. Finally, the tip was annealed.

The details of the fabrication process;

- Electron Bomberdment (EB) heating treatment
- Deposition of Fe
- Post annealing

, are described below.

### 3.2.1 Modification of normal Omicron tip holder for VT-STM

Figure. 3.3(a) shows Omicron official tip holder, and (b) shows a modified tip holder for VT-STM. For the fabrication of spin-polarized tip, it is needed that the apex of W-tip is heated up to 2200 K. On the case of Omicron official tip holder as shown in Fig. 3.3(a), it is difficult to access the tip apex, and thus it is difficult

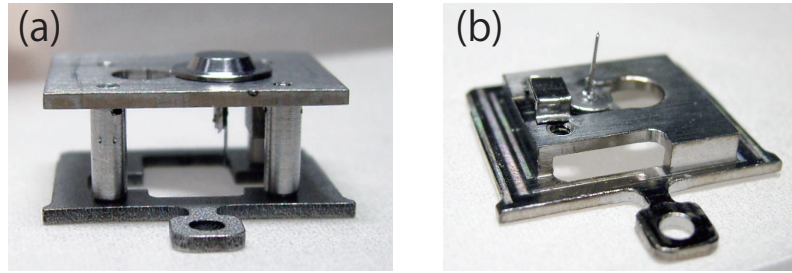


**Figure 3.3** (a)Omicron official tip holder for VT-STM, (b)Modified tip holder for VT-STM

to do high temperature heating treatment and deposition of Fe film. We modified the official tip holder in order to resolve these fault, and fabricated new tip holder which has easy accessibility to the tip apex as shown in Fig. 3.3(b). In this study, we use this modified tip holder.

### **3.3 Electron Bomberdment (EB) heating treatment**

Figure 3.4 shows the simplified circuit diagram for EB heating. High voltage is applied to the tip and the filament. Thermal electrons are ejected from the filament by causing a current to flow through it. The thermal electrons are accelerated by the electric field between the tip and the filament, and collide with the tip apex. As a result, the tip apex is heated up to about 2200 K, thus impurities and oxide film on the tip apex are vaporize. At this time, to give an effective thermal treatment of the tip apex, the tip was attached so that the length of the tip is 5 mm as shown in Fig.3.5(a) and the positions of the tip and filament were set so that the tip was insert about 1~2 mm into the filament as shown in Fig.3.5(b). High voltage of 500 V was applied to the tip, and EB heating was carried out for 15 sec so that the emission current flowing across the tip and the filament is kept at 70~80 mA.

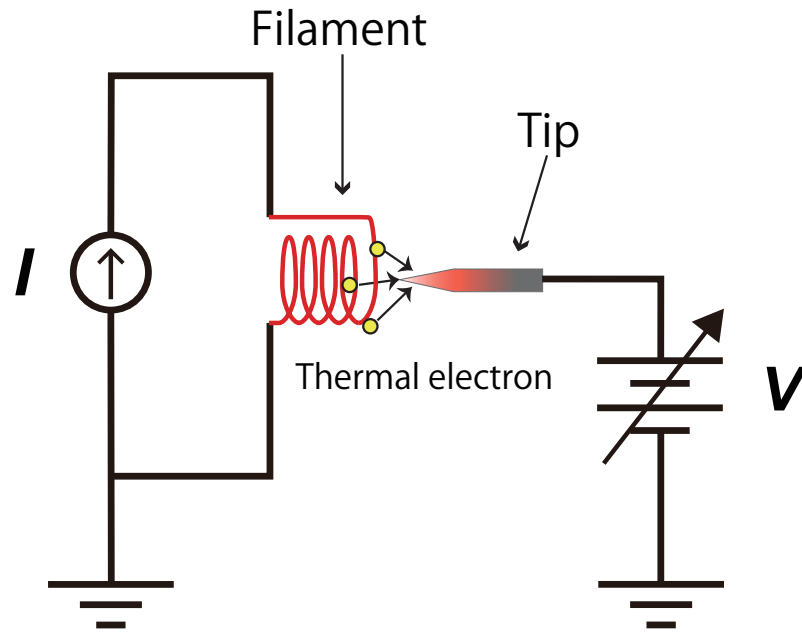


Figure 3.4 Circuit diagram for EB heating

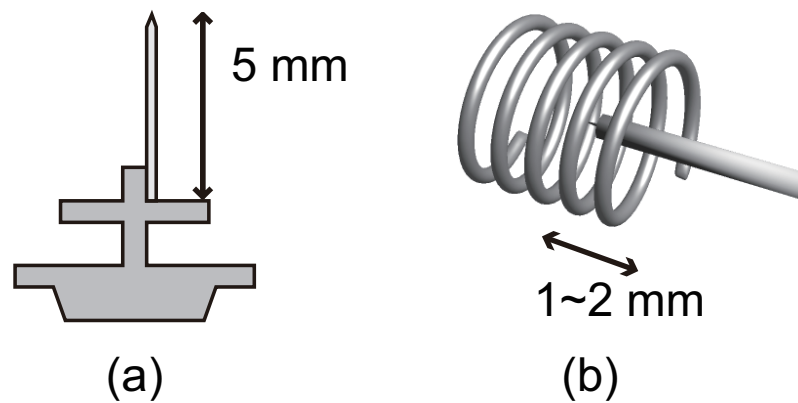
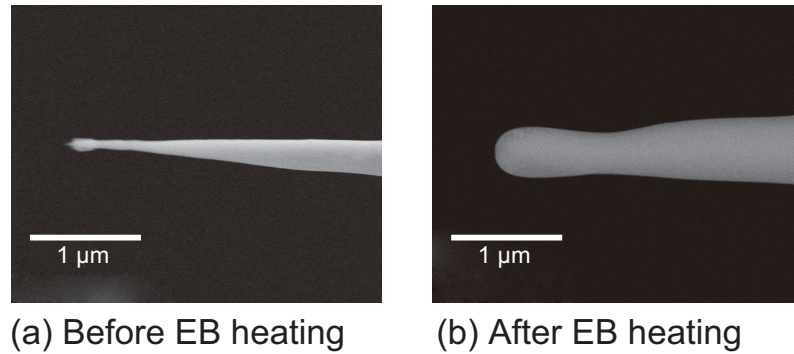


Figure 3.5 (a) Mounting position of a tip, (b) Positional relationship between tip and filament.



**Figure 3.6** SEM images of the tip. (a) Before EB heating, (b) After EB heating

After EB heating treatment, we checked the curvature radius ( $R$ ) of tips by SEM. Figure 3.6(a) is the SEM image of the tip before EB heating. It is seen that the  $R$  of the tip is less than 50 nm. On the other hand, it is clearly observed that the  $R$  of the tip got larger (about 250 nm) after EB hearing.

### 3.4 Deposition of Fe

After the EB heating, Fe was deposited on the tip apex by EFM3 at 1 ML/min for 30 min in a vacuum of  $5 \times 10^{-10}$  mbar at room temperature.

### 3.5 Post annealing

After the Fe deposition, the tip inserted into the filament at 1.2 mm and heated by filament. The filament was annealed by applying a DC current of 1.5 A for 5 min. This post annealing conducted by thermal radiation of the filament without applying High voltage between the tip and the filament.

### 3.6 Standard specimen: Cr(001) single crystal

We adopt Cr(001) single crystal as the standard specimen of SP-STs measurements. The Cr(001) is known that it is easy to get an atomically flat surface by some cleaning process and its surface exhibits the topological antiferromagnetism (i.e. magnetic moments of the atomically at terraces couple parallel but the adjacent terraces that are separated by a monoatomic step are magnetized antiparallel.) [73, 74]. For this reason, it has been reported that the  $dI/dV$  image which has spin contrast reversed on every terraces was observed [74].

### 3.7 Cleaning method of the standard specimen: Cr(001) single crystal cleaning

The spin-polarized d-like surface state locates close to the Fermi level on the clean Cr(001) as shown in Fig. 3.7 [3]. However, the peak does not obtained in the case of that the cleaning of the surface is insufficient. Therefore, Cr(001) single crystal surface is cleaned by repeated cycles of Ar<sup>+</sup> ion sputtering and annealing until the  $dI/dV$  curve which has the peak obtained. The details of the fabrication process are described below.

- (1) Ar<sup>+</sup> ion sputtering with annealing (Annealing temperature:  $T_s$ )
- (2) Ar<sup>+</sup> ion sputtering at RT
- (3) Post annealing (Annealing temperature:  $T_a$ )

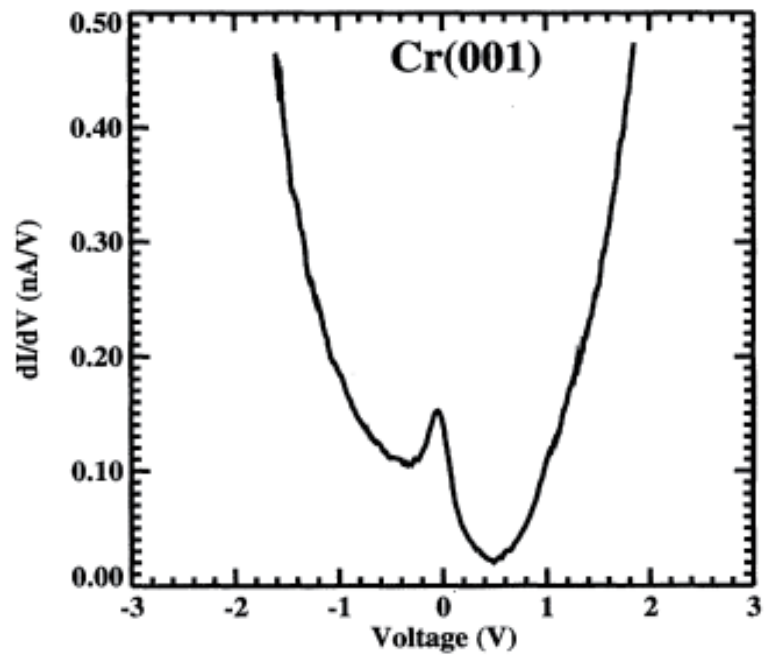


Figure 3.7 Tunneling conductance vs sample voltage measurements of the Cr(001) surface obtained at constant height above the Fe surface.(after figure 5 in Ref. [3])

# Chapter 4

## Results and Discussion

### 4.1 Cr(001) single crystal cleaning

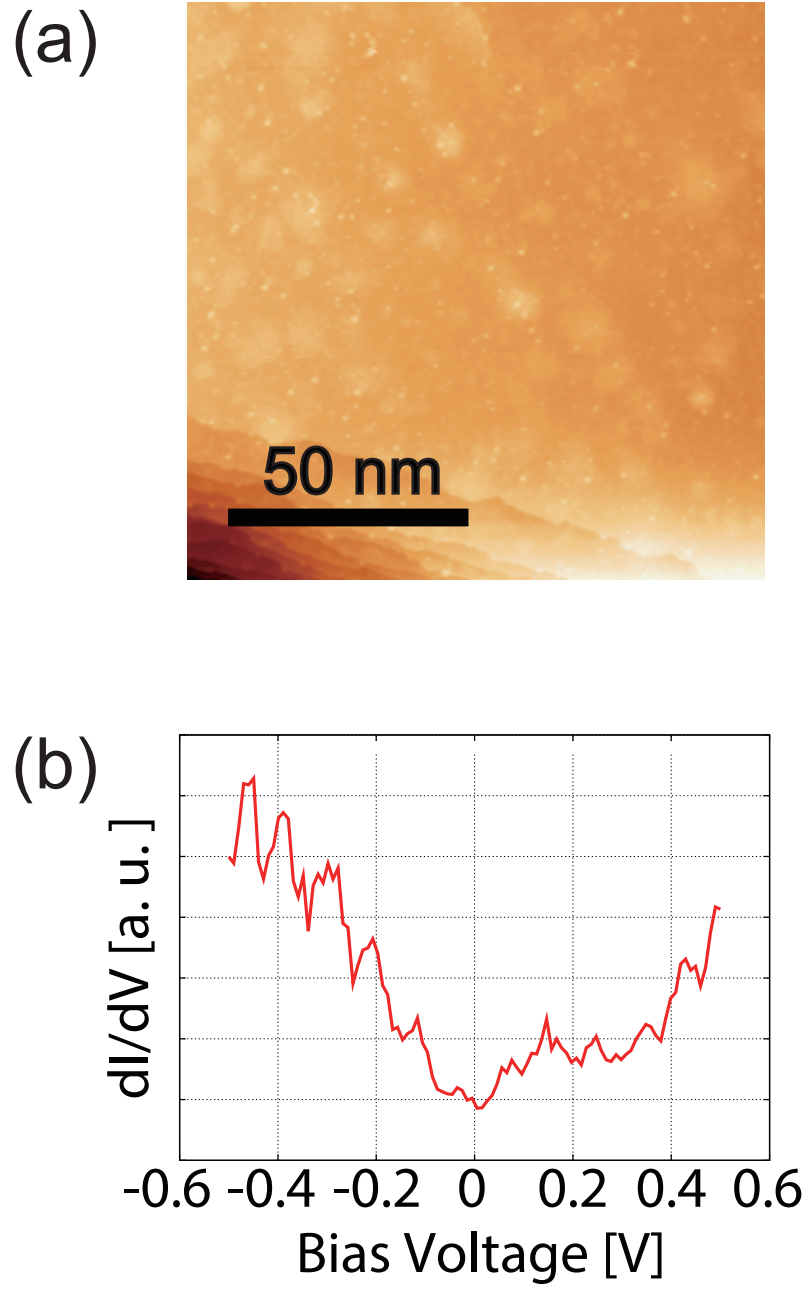
We conducted the cleaning of Cr(001) surface with four different conditions. The cleaning conditions of Ar<sup>+</sup> ion sputtering and annealing temperature are shown in table 4.1 and 4.2. Figure 4.1-4.4 are STM images and  $dI/dV - V$  curves taken on the Cr(001) surface after each cleaning condition A, B, C and D, respectively. In the case of condition A, as can be seen from Fig. 4.1, there were some contamination on the surface, and  $dI/dV$  curve does not show the peak around Fermi level. In the case of condition B, it can be seen that the width of the terraces were 10-20 nm and the  $dI/dV$  curve shows the peak around energy level of 0.1 V (see in Fig. 4.2). In the case of condition C, the results in Fig. 4.3 indicate that the width of the terraces were about 100 nm and the  $dI/dV$  curve shows the peak around Fermi level. Moreover, the surface which has monoatomic terraces was clearly observed. It is needed for SP-STs measurements of Cr(001) surface. In the case of condition D, as can be seen from Fig. 4.4, there were some contamination on the surface, though  $dI/dV$  curve shows the peak around Fermi level. These results indicate that the cleaning condition C is appropriate cleaning condition in order to conduct SP-STs measurements. We adopted the condition C and obtained clean Cr(001) surface with high reproducibility.

**Table 4.1** Cleaning condition of Ar<sup>+</sup> ion sputtering

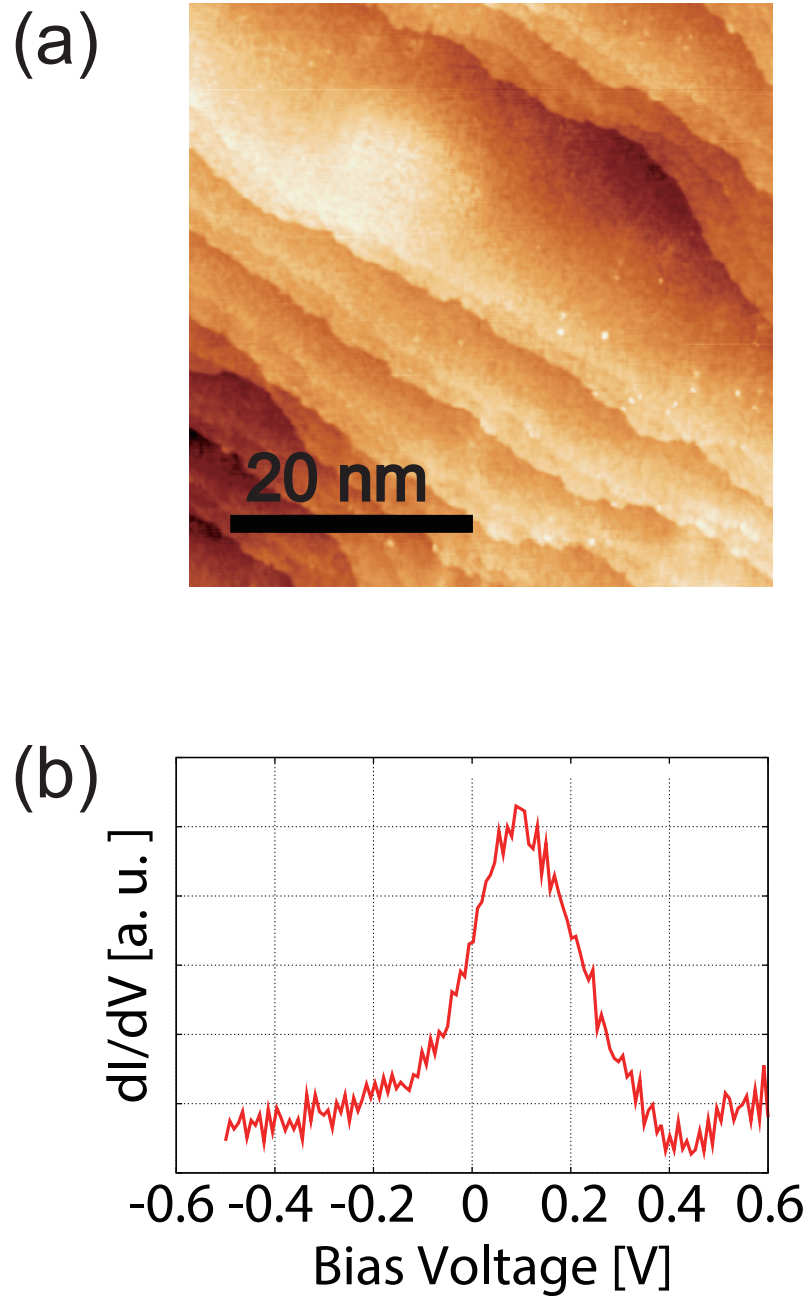
Cleaning	Acceleration voltage [kV]	Ar Pressure [mPa]
(1)Ar <sup>+</sup> ion sputtering with annealing	1.0	11
(2)Ar <sup>+</sup> ion sputtering at RT	1.5	11

**Table 4.2** Cleaning condition (Annealing temperature)

Cleaning condition	$T_s$ [°C]	$T_a$ [°C]
A	(RT)	700
B	700	700
C	820	800
D	840	800



**Figure 4.1** (a) STM image of Cr(001) single crystal surface ( $I_t = 0.3$  nA,  $V_s = 0.8$  V), (b)  $dI/dV$  curve taken at the terrace.



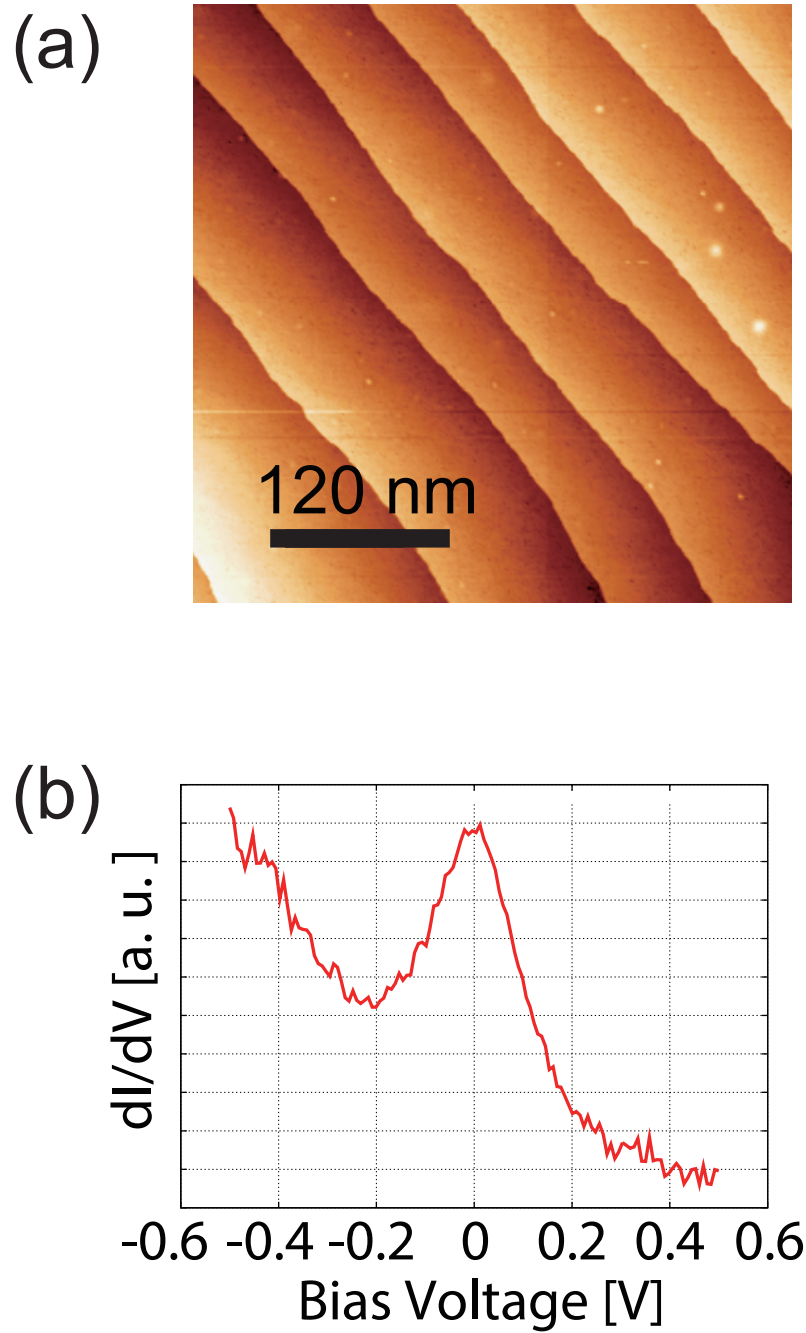


**Figure 4.3** (a) STM image of Cr(001) single crystal surface ( $I_t = 0.3$  nA,  $V_s = -0.12$  V), (b)  $dI/dV$  curve taken at the terrace.

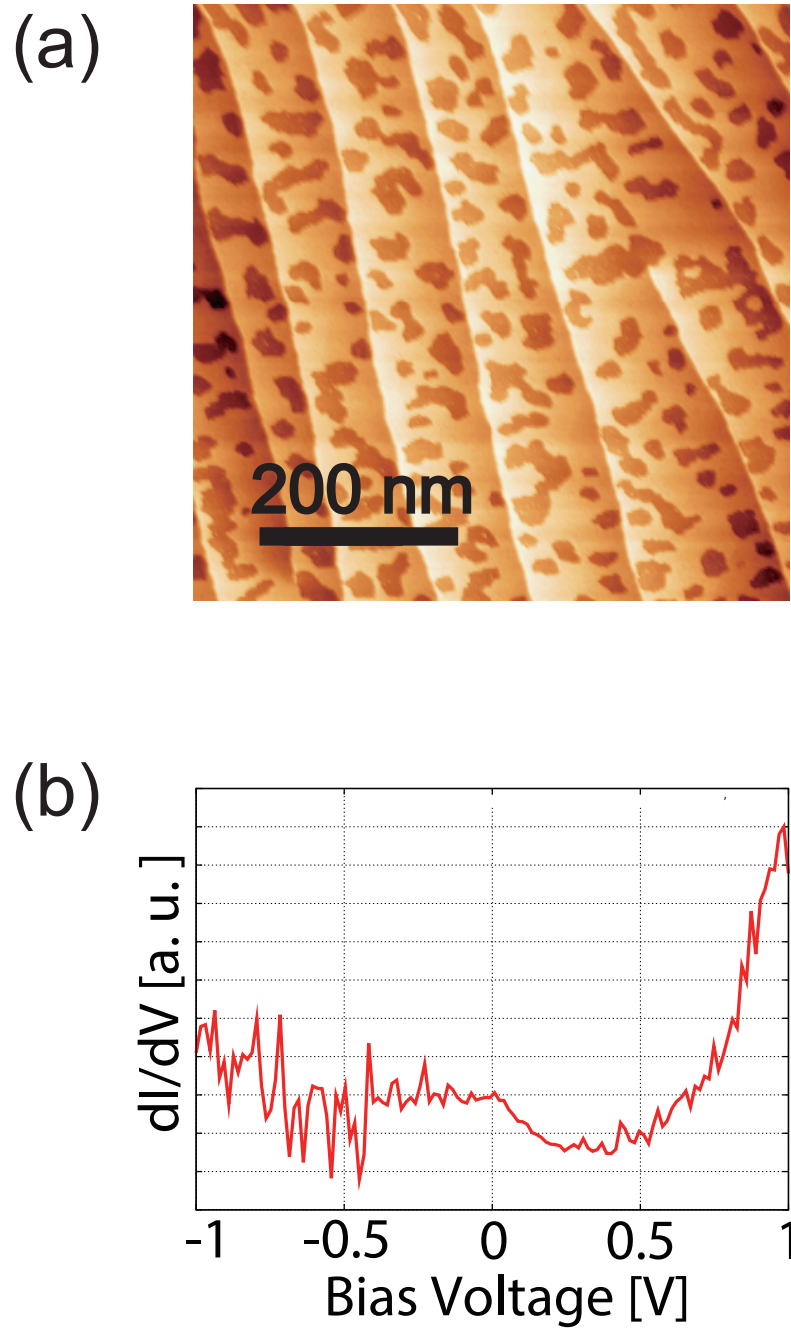
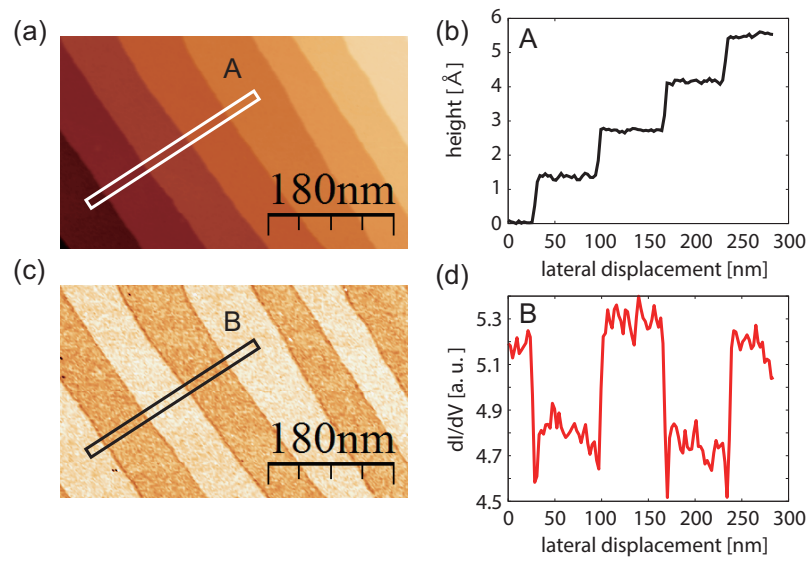


Figure 4.4 (a) STM image of Cr(001) single crystal surface ( $I_t = 0.3$  nA,  $V_s = -0.1$  V), (b)  $dI/dV$  curve taken at the terrace.

## 4.2 SP-STs measurements of Cr(001) by Fe/W tip

We carried out SP-STs measurements of Cr(001) surface with the Fe coated W tip. STs results were acquired using a phase-sensitive detection technique with a bias modulation of 20 mV at 5.23 kHz. Figure 4.5(a) is the STM image of the Cr(001) surface, and Fig.4.5(c) is the  $dI/dV$  conductance map taken simultaneously with the STM image. Figure 4.5(b) and (d) are cross sectional line profile along area A and B, respectively. As can be seen from Fig. 4.5(c), atomically flat terraces and monoatomic steps (1.45 Å) are observed. The same step terrace structure was clearly observed in  $dI/dV$  map shown in Fig. 4.5(c). According to the  $dI/dV$  map and the cross sectional line profile shown in Fig.4.5(d), mutually adjacent terraces have different values of  $dI/dV$ . A SP-STs study with a Fe coated W tip should be sensitive to the alternating magnetization of the (001) terraces. Consequently, it can be said that the Fe coated W tip is spin-polarized.



**Figure 4.5** Results of SP-STIS measurement on Cr(001) single crystal surface with Fe coted W tip at a tunneling current of 360 pA and a bias voltage of -170 mV. (a) Topographic image of Cr(001) single crystal surface. (b)  $dI/dV$  map at a bias voltage of -170 mV for the same region shown in (a). (c) Line profiles of the topography and the  $dI/dV$  signal taken along the white rectangle in (a) and black rectangle in (b). The relative position of the rectangles is same.

## Part II

Surface atomic configurations  
around antiphase domain  
boundaries in  $\text{Fe}_3\text{O}_4$  films on  
 $\text{MgO}(001)$



# Abstract

In this part, the STM/STS experiments of  $\text{Fe}_3\text{O}_4(001)$  films on  $\text{MgO}(001)$  substrate will be summarized. We have studied the surface atomic configurations around antiphase domain boundaries (APBs) in epitaxial magnetite ( $\text{Fe}_3\text{O}_4$ ) thin films on  $\text{MgO}(001)$  by scanning tunneling microscopy (STM). The observed surface of the  $\text{Fe}_3\text{O}_4$  films is the B-plane terminating surface with the  $(\sqrt{2} \times \sqrt{2})R45^\circ$  reconstruction. Several variations of APBs are observed by STM at atomic resolution. The observed APBs are categorized into a APBs labeled by three different phase shift vectors: in-plane  $1/4[110]$ , in-plane  $1/2[100]$ , and out-of-plane  $1/4[101]$ . We discussed how these APBs appear on the surface. The proportions of the APBs with  $1/4[110]$ ,  $1/2[100]$ , and  $1/4[101]$  shifts are about 38%, 1%, and 61%, respectively, in our experiment.

# Chapter 5

## Introduction

Magnetite ( $\text{Fe}_3\text{O}_4$ ) has been attracting much attention because of its electrical and magnetic properties such as half-metallicity and a high Curie temperature of 858 K [9, 10, 75]. From the viewpoint of its application to spin-related devices, thin films of  $\text{Fe}_3\text{O}_4$  are also interesting because they have fascinating potential properties that could provide highly spin-polarized electrodes for such devices. However,  $\text{Fe}_3\text{O}_4$  films grown epitaxially on MgO substrates (MgO is an insulating material often used in spin-sensitive devices) contain a high density of antiphase domain boundaries (APBs) [14, 76, 77]. These APBs make the electrical and magnetic properties of the films complicated. For example, APB-induced magnetic domains as small as 5 to 10 nm were studied by Lorentz microscopy [78]. The atomic configurations of APBs in an epitaxial  $\text{Fe}_3\text{O}_4(110)$  films and its effects on their magnetic properties have been discussed [79]. In addition to these reports, it has recently been reported that APBs can induce inhomogeneous electronic properties on the surface of  $\text{Fe}_3\text{O}_4(001)$  [37]. Therefore, it would also be interesting to study the effects of APBs on surface electronic states as well as on magnetic properties.

APBs with seven different shift vectors can exist in epitaxial  $\text{Fe}_3\text{O}_4$  layers [76]. Seven different types of APBs in the bulk films have been observed, and the atomic configurations of the APBs have been discussed [77]. However, there have been no reports yet on the surface atomic configurations of APBs in the film surface of  $\text{Fe}_3\text{O}_4(001)$ . We have used scanning tunneling microscopy (STM) to identify the atomic structures of the APBs. In this part, we report STM studies of epitaxial  $\text{Fe}_3\text{O}_4$  films on MgO(001) and reveal the surface atomic configurations around APBs.

## 5.1 Crystal structure and Surface reconstruction of $\text{Fe}_3\text{O}_4$

Bulk  $\text{Fe}_3\text{O}_4$  has a cubic inverse spinel structure with a lattice constant of 8.397 Å. In the [001] direction, A layers of tetrahedral iron ( $\text{Fe}_A$ ) and B layers containing oxygen and octahedral iron ( $\text{Fe}_B$ ) are stacked alternately as shown in Fig. 5.1(a). A B-terminated surface with the  $(\sqrt{2} \times \sqrt{2})R45^\circ$  reconstruction has often been observed on the  $\text{Fe}_3\text{O}_4(001)$  surface by STM [32, 34, 80]. Several models have been proposed to explain this reconstruction on the basis of the formation of  $\text{Fe}^{2+}\text{-Fe}^{2+}$  and  $\text{Fe}^{3+}\text{-Fe}^{3+}$  pairs along the  $\text{Fe}_B$  rows [34], B layer termination with one oxygen vacancy per unit cell [32, 81], Jahn-Teller distortion in the B-terminated surface [4], or cation vacancy in the B-terminated surface [33].

## 5.2 Antiphase domain boundary (APB)

It is well known that epitaxially grown  $\text{Fe}_3\text{O}_4$  films on  $\text{MgO}(001)$  substrate contain a high density of anti-phase domain boundaries (APBs), these APBs make the electrical and magnetic properties of the films complicated. The APB is a type of stacking fault with shift vector  $\mathbf{R}$  relating adjacent domains, and the domains separated by the APBs are called anti-phase domains (APDs).

### 5.2.1 Formation of the APBs in $\text{Fe}_3\text{O}_4$ films on $\text{MgO}(001)$

In the case of deposition of  $\text{Fe}_3\text{O}_4$ ,  $\text{MgO}(001)$  is used as the substrates in our experiments because of its small lattice mismatch (0.3%). A lattice constant of  $\text{MgO}$  is 0.4212 nm, and a lattice constant of  $\text{Fe}_3\text{O}_4$  is 0.8397 nm. Additionally, the crystal structure of  $\text{MgO}(001)$  has fourfold rotational symmetry, and  $\text{Fe}_3\text{O}_4(001)$  has twofold rotational symmetry. Because of the difference in lattice constant and crystal symmetry, the different islands which shifted with shift vector  $\mathbf{R}$  each other

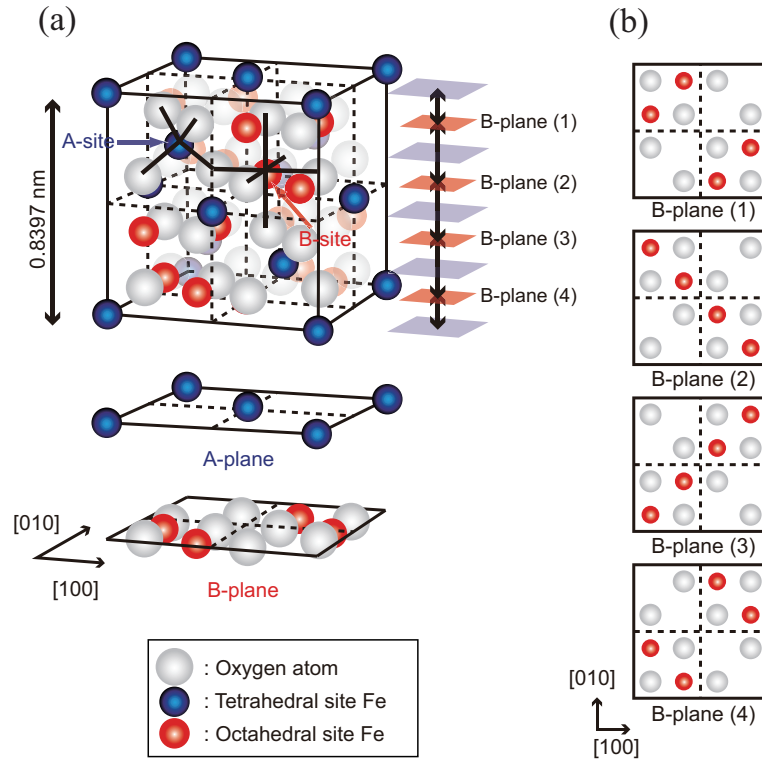


**Figure 5.1** (a) Cubic inverse spinel structure of  $\text{Fe}_3\text{O}_4$ . Tetrahedral iron ( $\text{Fe}_A$ ) in the A-plane, a octahedral iron ( $\text{Fe}_B$ ) in the B-plane, and oxygen are indicated by a reddish circle, a bluish circle, and a grayish circle, respectively. (b) Four possible types of surface unit cells in unrelaxed B-plane termination  $\text{Fe}_3\text{O}_4(001)$  surfaces. Precise surface relaxation should be considered, and surface unit cells do not coincide with the actual unit cell on the surfaces. However, it is convenient to use these unit cells for understanding atomic arrangements around APBs.

can be formed in the first stages of growth of  $\text{Fe}_3\text{O}_4$  on  $\text{MgO}(001)$  (see in fig.5.2). Then APBs form when such islands of  $\text{Fe}_3\text{O}_4(001)$  coalesce. In the fig.5.2, base  $\text{Fe}_3\text{O}_4(001)$  monolayer (island A) and two adjacent  $\text{Fe}_3\text{O}_4(001)$  monolayer shifted by  $1/2[010]$  (island C) and  $1/4[110]$  (or  $1/4[1\bar{1}0]$ ) (island D) are illustrated. These  $1/2[010]$ ,  $1/4[110]$  and  $1/4[1\bar{1}0]$  shift type of APBs are called in-plane shifts APBs [76]. Another  $\text{Fe}_3\text{O}_4(001)$  monolayer, island B, shows different type of shift. It is a result of the lower symmetry of  $\text{Fe}_3\text{O}_4(001)$  monolayers compared to the  $\text{MgO}(001)$

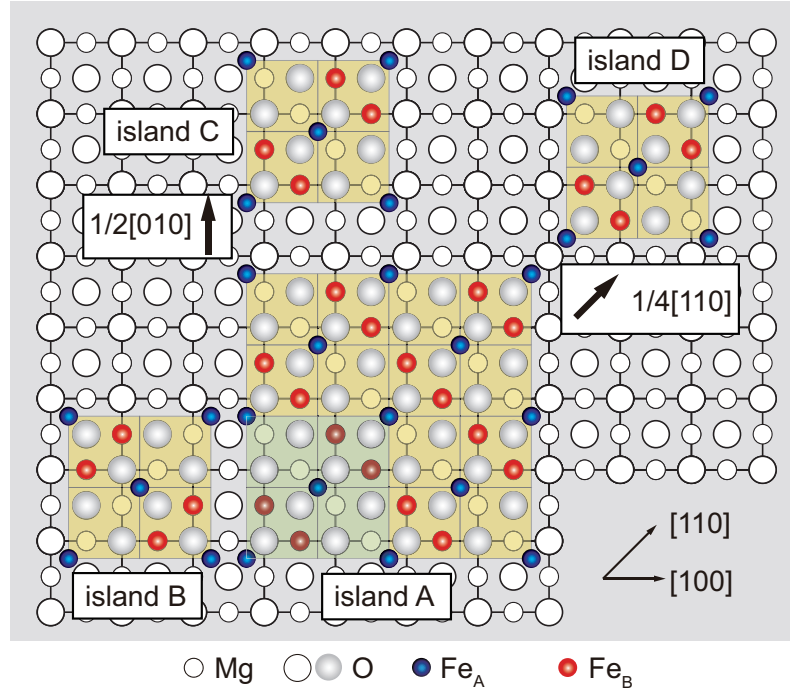


**Figure 5.2** First monolayer of  $\text{Fe}_3\text{O}_4$  on  $\text{MgO}(001)$  substrate.

substrate. The  $\text{Fe}_3\text{O}_4$  monolayer of island B is rotated by  $90^\circ$  compared to the island A. This type of shift is classified the  $1/4[101]$  (or  $1/4[10\bar{1}]$ ,  $1/4[011]$ , and  $1/4[01\bar{1}]$ ), and these type of APBs are called out-of-plane shifts APBs [76].

### 5.2.2 Atomic structures around APBs on the $\text{Fe}_3\text{O}_4(001)$ films surface

The APBs are distinguished by seven different shift vectors as described above. The  $1/4[110]$ ,  $1/4[1\bar{1}0]$ , and  $1/2[100]$  shifts ( $1/4[101]$ ,  $1/4[10\bar{1}]$ ,  $1/4[011]$ , and  $1/4[01\bar{1}]$  shifts) are classified as in-plane shifts (out-of-plane shifts). The atomic structure of the  $1/4[110]$  shift ( $1/4[101]$  shift) is equivalent to that of the  $1/4[1\bar{1}0]$  shift ( $1/4[10\bar{1}]$ ,  $1/4[011]$ , and  $1/4[01\bar{1}]$  shifts). Therefore, here we describe only the  $1/4[110]$ ,  $1/2[100]$ , and  $1/4[101]$  shifts.

**in-plane  $1/4[110]$  shift**

Figure 5.3 shows the atomic structure models near the APB with  $1/4[110]$  shift vector. In the figure, topmost B-plane, A-plane below the top most B-plane, and second B-plane of the  $\text{Fe}_3\text{O}_4(001)$  are illustrated. Tetrahedral iron ( $\text{Fe}_A$ ) in the A-plane, a octahedral iron ( $\text{Fe}_B$ ) in the B-plane, and oxygen are indicated by a reddish circle, a bluish circle, and a grayish circle, respectively. As indicated in Fig. 5.1, there are four B-planes (B-plane (1), (2), (3), (4)). Therefore, in the Fig. 5.3, four atomic structure models which each B-plane is set as the reference plane are illustrated. The unit cell of the reference plane is highlighted as blue color. According to Fig. 5.3(a)-(d), each model has different periodic structure of  $\text{Fe}_A$  and  $\text{Fe}_B$ . Here it can be seen that four different surface atomic structures are observable in the STM measurements.

**in-plane  $1/2[100]$  shift**

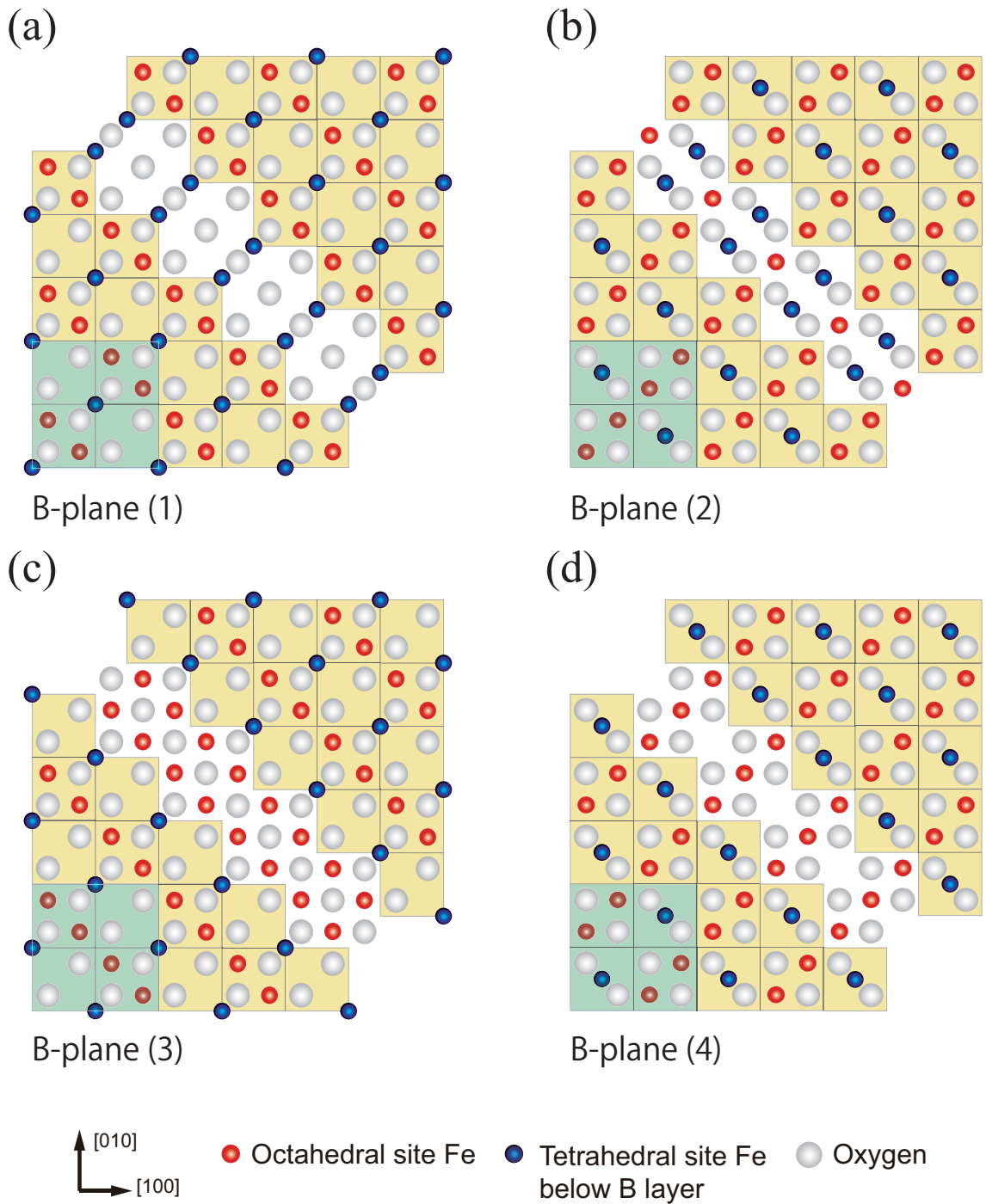
Figure 5.4 shows the atomic structure models near the APB with  $1/2[100]$  shift vector. As indicated in Fig. 5.4(a)-(d), the atomic structure of Fig. 5.4(a) is equivalent to that of Fig. 5.4(c). Similarly, the atomic structure of Fig. 5.4(b) is equivalent to that of Fig. 5.4(d). Therefore, it is expected that two different surface atomic structures are observable in the STM measurements.

**out-of-plane  $1/4[101]$  shift**

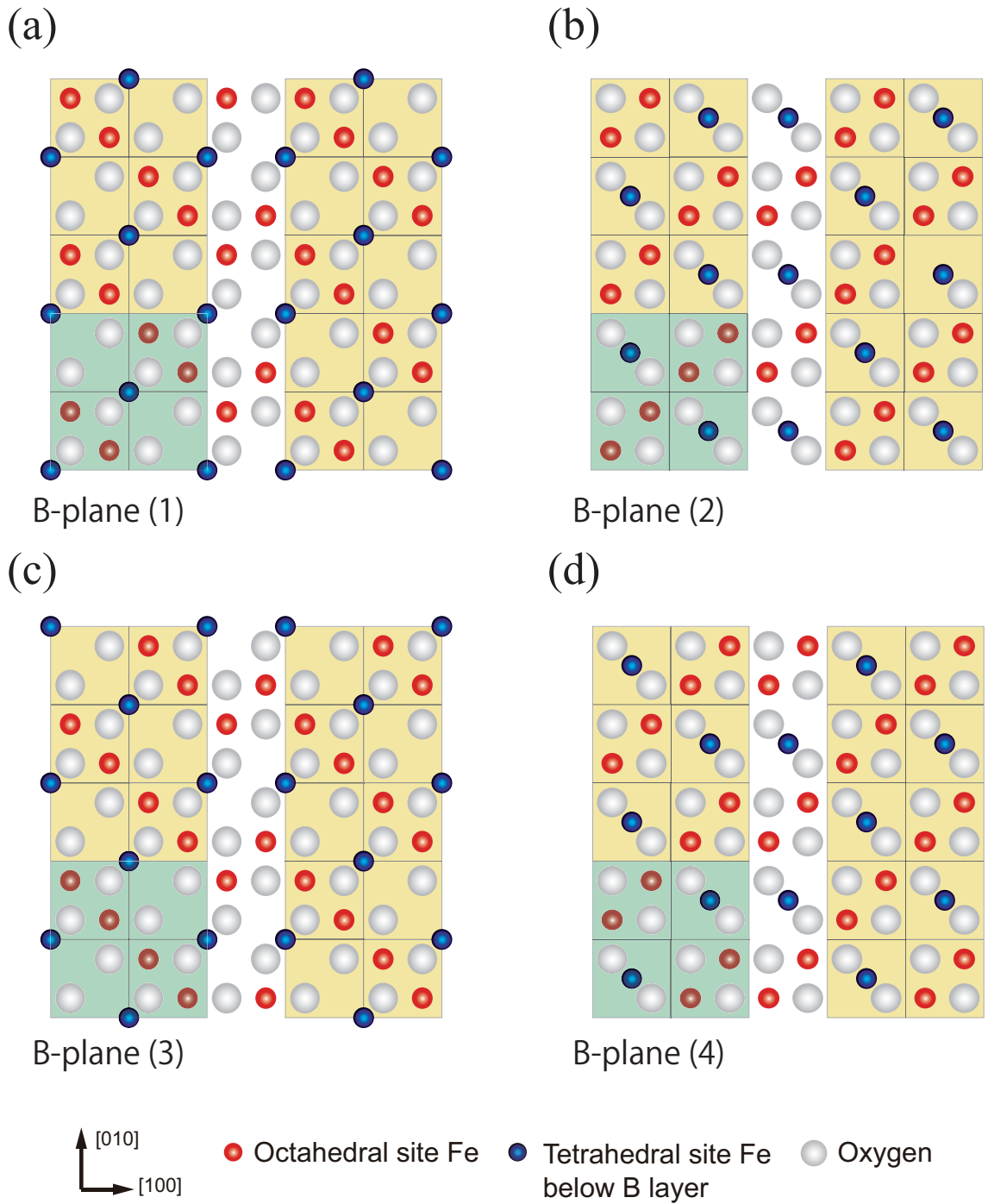
Figure 5.5 shows the atomic structure models near the APB with  $1/4[101]$  shift vector. As indicated in Fig. 5.5(a)-(d), the atomic structure of Fig. 5.5(a) is equivalent to that of Fig. 5.5(c). Similarly, the atomic structure of Fig. 5.5(b) is equivalent to that of Fig. 5.5(d). Therefore, it is expected that two different surface atomic structures are observable in the STM measurements.

Figure 5.5 is the models which the APB is induced along  $[010]$  direction. In reality,

however, the APB inducing along  $[130]$  direction has often observed by STM and TEM studies [13, 37, 77]. Figure 5.6 shows the atomic structure models near the such APB.



**Figure 5.3** Atomic structure models near the APB with  $1/4[110]$  shift vector. (a) shows the first oxygen layer with octahedral sites and the tetrahedral sites directly below this plane and (b), (c) and (d) show the second third and fourth layer respectively.



**Figure 5.4** Atomic structure models near the APB with  $1/2[100]$  shift vector. (a) shows the first oxygen layer with octahedral sites and the tetrahedral sites directly below this plane and (b), (c) and (d) show the second third and fourth layer respectively.

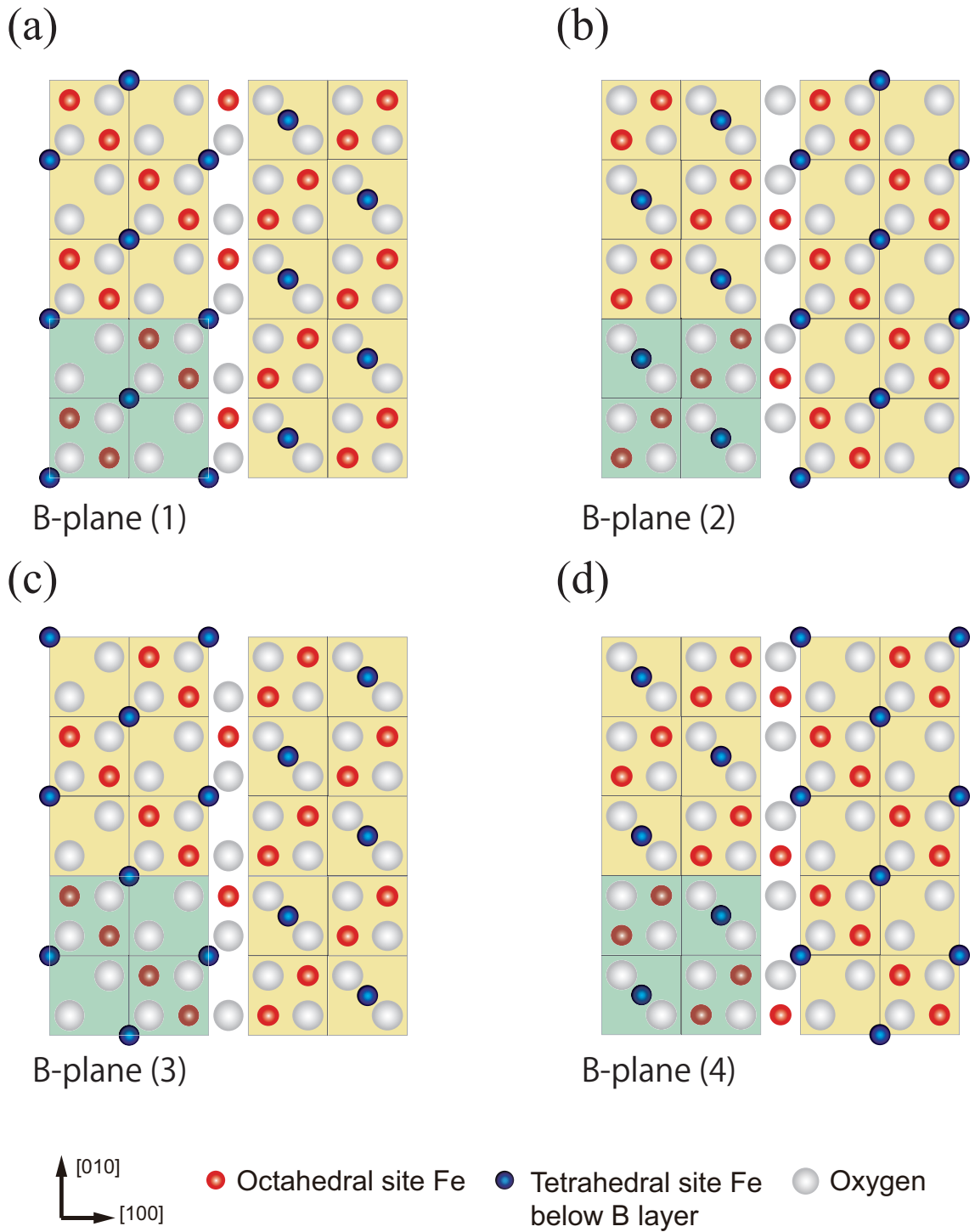
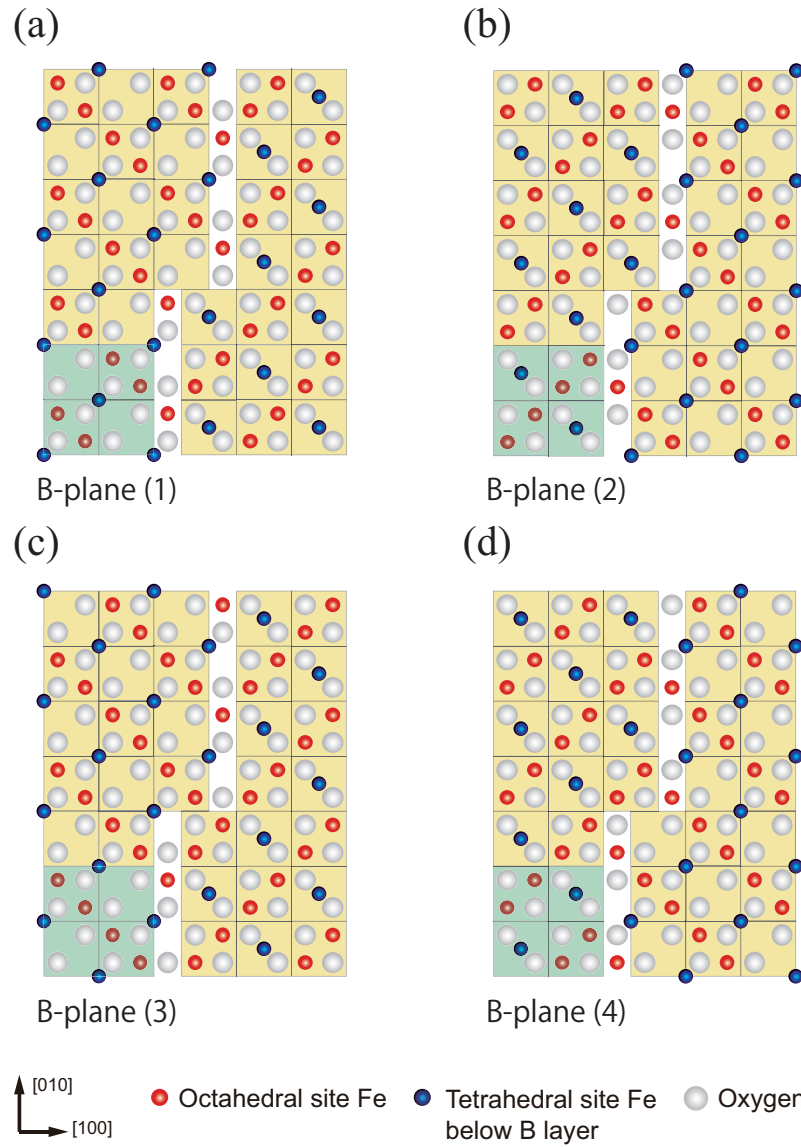


Figure 5.5 Atomic structure models near the APB with  $1/4[101]$  shift vector and (010) boundary plane. (a) shows the first oxygen layer with octahedral sites and the tetrahedral sites directly below this plane and (b), (c) and (d) show the second third and fourth layer respectively.



**Figure 5.6** Atomic structure models near the APB with  $1/4[101]$  shift vector and  $(130)$  boundary plane. (a) shows the first oxygen layer with octahedral sites and the tetrahedral sites directly below this plane and (b), (c) and (d) show the second third and fourth layer respectively.

**Table 5.1** Magnetic exchange interactions in ideal bulk  $\text{Fe}_3\text{O}_4$ , listed according to their relative strength.

Label	Exchange interaction	Type	angle [deg]	Sign	Strength
I	$\text{Fe}_B\text{-O-Fe}_A$	super	$\sim 120$	AF	strong
II	$\text{Fe}_B\text{-O-Fe}_B$	super	90	FM	weak
III	$\text{Fe}_B\text{-Fe}_B$	direct		FM	weak

### 5.2.3 Magnetic coupling in $\text{Fe}_3\text{O}_4$ films

It is expected that the atomic arrangement of Fe and O atoms adjacent to the APBs are different from that of the bulk  $\text{Fe}_3\text{O}_4$ . The atomic arrangement and interval differ depending on the type of the APBs. The magnetic frustration arises from the APBs, and it causes formation of inhomogeneous magnetic domain. There have been predictions for the exchange interaction between Fe atoms adjacent to the APBs based on a geometric arrangement relation of the atoms [77,82,83]. According to these studies, three types of the magnetic interaction are exist in ideal bulk  $\text{Fe}_3\text{O}_4$  as described below and shown in Table 5.1.

- $\text{Fe}_B\text{-O-Fe}_A$  ( $\sim 120^\circ$ ), superexchange interaction, Anti-ferromagnetic(AF) coupling (labeled I)
- $\text{Fe}_B\text{-O-Fe}_B$  ( $90^\circ$ ), superexchange interaction, Ferromagnetic(FM) coupling (labeled II)
- $\text{Fe}_B\text{-Fe}_B$ , double exchange interaction, FM coupling (labeled III)

Figure 5.7 shows the relationship among the atomic arrangements, the magnetic coupling and the directions of magnetic moment. As can be seen in Fig. 5.7, each

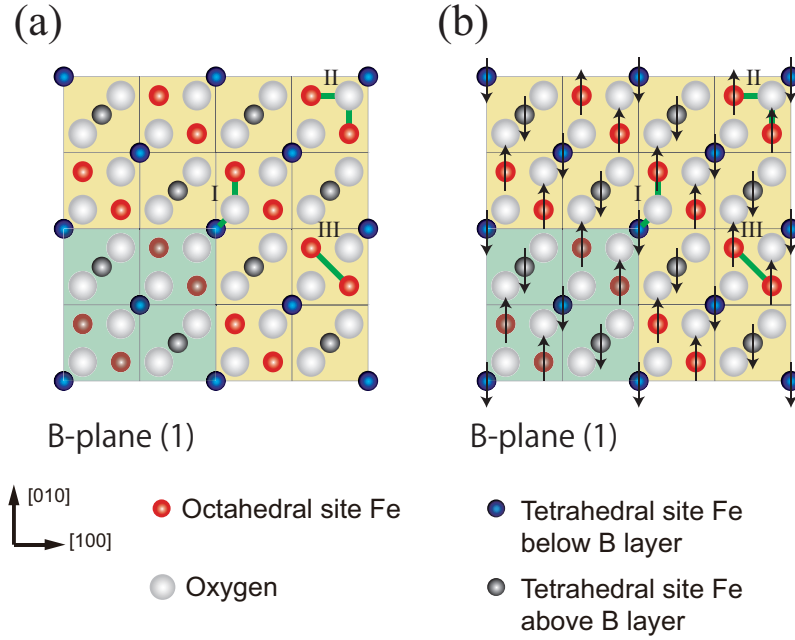


**Figure 5.7** Atomic structure models of ideal bulk  $\text{Fe}_3\text{O}_4$ . (a) and (b) show the first oxygen layer with octahedral sites and the tetrahedral sites directly below this plane. Examples of magnetic couplings are indicated as green lines. The directions of the spin are indicated as black arrows.

$\text{Fe}_B$  atoms are arranged ferromagnetically, and each  $\text{Fe}_A$  atoms are also arranged ferromagnetically. However,  $\text{Fe}_A$  and  $\text{Fe}_B$  are arranged anti-ferromagnetically each other. According to the Hund's rule,  $\text{Fe}^{3+}$  atoms ( $\text{Fe}_A$ ,  $\text{Fe}_B$ ) have a magnetic moment of  $5 \mu_B$ , and  $\text{Fe}^{2+}$  atoms ( $\text{Fe}_B$ ) have a magnetic moment of  $4 \mu_B$ . Hence,  $\text{Fe}_3\text{O}_4$  shows the ferromagnetism [75]. However, in the case of  $\text{Fe}_3\text{O}_4$  films induced the APBs, it is necessary to consider five new magnetic coupling besides the three magnetic coupling described above. We describe these five types of magnetic coupling below.

- $\text{Fe}_B\text{-O-Fe}_B$  ( $180^\circ$ ), superexchange interaction, AF coupling (labeled IV)
- $\text{Fe}_A\text{-O-Fe}_A$  ( $\sim 140^\circ$ ), superexchange interaction, AF coupling (labeled V)
- $\text{Fe}_A\text{-O-Fe}_A$  ( $\sim 70^\circ$ ), superexchange interaction, AF coupling (labeled VIII)

**Table 5.2** Magnetic exchange interactions across APBs in  $\text{Fe}_3\text{O}_4$  films on  $\text{MgO}$ , listed according to their relative strength.

Label	Exchange interaction	Type	angle [deg]	Sign	Strength	Presence
IV	$\text{Fe}_B\text{-O-Fe}_B$	super	180	AF	strong	at APB
V	$\text{Fe}_A\text{-O-Fe}_A$	super	$\sim 140$	AF	strong	at APB
VI	$\text{Fe}_B\text{-O-Fe}_A$	super	$\sim 120$	AF	strong	bulk and at APB
VII	$\text{Fe}_B\text{-O-Fe}_B$	super	90	FM	weak	bulk and at APB
VIII	$\text{Fe}_A\text{-O-Fe}_A$	super	$\sim 70$	AF	weak	at APB
IX	$\text{Fe}_B\text{-Fe}_B$	direct		FM	weak	bulk and at APB
X	$\text{Fe}_A\text{-Fe}_A$	direct		AF	weak	at APB
XI	$\text{Fe}_B\text{-Fe}_A$	direct		FM	weak	at APB

- $\text{Fe}_A\text{-Fe}_A$ , double exchange interaction, AF coupling (labeled X)
- $\text{Fe}_B\text{-Fe}_A$ , double exchange interaction, FM coupling (labeled XI)

Figure 5.8 shows the atomic arrangements and the magnetic coupling adjacent to the APB with  $1/4[101]$  shift vector. In this case, there are four types of the magnetic coupling, type IV, V, VI, VII, adjacent to the APB. These magnetic frustrations cause formation of inhomogeneous magnetic domain. Recently, McKenna *et al.* have reported that the APB with  $1/4[110]$  shift vector induce antiferromagnetic coupling between adjacent domains by using DFT calculation.

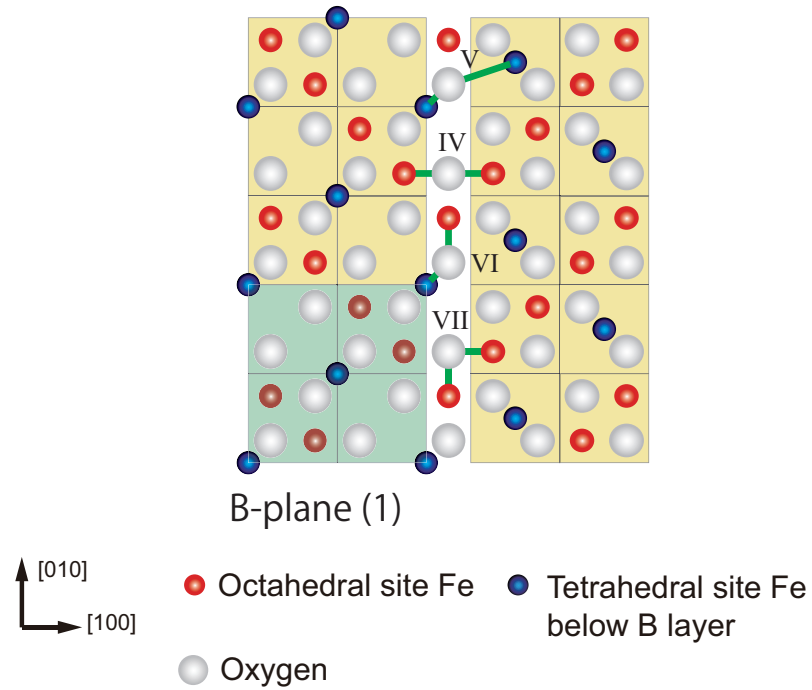


**Figure 5.8** Atomic structure models near the APB with  $1/4[101]$  shift vector and  $(010)$  boundary plane. Figure shows the first oxygen layer with octahedral sites and the tetrahedral sites directly below this plane. Examples of magnetic superexchange interactions across the boundary are indicated as green lines.

# Chapter 6

## Experimental

The experiments were carried out in an ultrahigh-vacuum (UHV) system with a base pressure of  $5 \times 10^{-11}$  mbar. The system has two chambers containing STM and molecular beam epitaxy (MBE) facilities as described in Chap. 3 in detail. STM/STS was performed at room temperature with W-tips. The W-tips were prepared by electrochemical etching and were subsequently flashed up to 2200 K by electron beam heating in the UHV. SP-STS was performed at room temperature with Cr/W-tips. The W-tips were prepared by electrochemical etching and were subsequently flashed up to 2200 K by electron beam heating in the UHV, then a Cr layer of 5 nm thick was deposited onto the W-tip. After that, the tip was annealed *in situ* for 5 min by thermal radiation of the filament, which is close to the tip [84]. STM images were acquired in a constant-current mode. A bias voltage was applied to the sample with respect to the grounded tip. The  $dI/dV$  signal was measured using a standard lock-in technique with a modulation signal of 20 mV<sub>rms</sub> at 5.24 kHz.

The epitaxially grown Fe<sub>3</sub>O<sub>4</sub>(001) thin films were prepared on MgO(001) single-crystal substrates by the deposition of Fe in the presence of oxygen. The MgO(001) substrates were cleaned *in situ* by heating at 573 K over 16 hours and then annealed at 1073 K for 1 hour in oxygen atmosphere ( $7 \times 10^{-7}$  mbar). The Fe deposition were performed using an electron-beam heating evaporator (Omicron EFM 3) at a substrate temperature of 573 K. During the film formation, the oxygen pressure was set in the range from  $7 \times 10^{-7}$  to  $1 \times 10^{-6}$  mbar. The growth rate was 0.9 ML/min and the film thickness was 20 nm [12, 13, 37, 40]. After the deposition, the grown

films were annealed at 573 K for 30 min in the same oxygen atmosphere.

# Chapter 7

## Results and Discussion

### 7.1 STM measurements of the surface atomic structure on Fe<sub>3</sub>O<sub>4</sub> films surface

An STM image of the epitaxially grown Fe<sub>3</sub>O<sub>4</sub>(001) surface is shown in Fig. 7.1(a). Atomically flat terraces can be seen. The minimum step height is  $\sim 0.21$  nm, as revealed by the line profile shown in Fig. 7.1(b). This step height corresponds to the A-A or B-B layer separation distance of Fe<sub>3</sub>O<sub>4</sub>. It indicates that the surface is terminated at the A-plane or B-plane. Additionally, we show a high-resolution STM image in Fig. 7.2. Rows running along [110] can be clearly seen. The distance between two rows is  $\sim 0.6$  nm, and the distance between two bright spots within the rows is  $\sim 0.3$  nm. Since the periodicities of  $\sim 0.6$  and  $\sim 0.3$  nm correspond to those of Fe<sub>B</sub> in the B-plane, each bright spot in the STM images should represent a single Fe<sub>B</sub>. Therefore, we conclude that the surface is terminated by the B-plane. STM also resolved the  $(\sqrt{2} \times \sqrt{2})R45^\circ$  reconstruction (indicated by the square in Fig. 7.2), which has been reported by several groups [32, 34, 80].

### 7.2 STM measurements of the surface atomic structure around the APBs

In this section, we discuss STM images of the Fe<sub>3</sub>O<sub>4</sub> surface that includes APBs and investigate models of the atomic configurations around the APBs. Models of APBs in the bulk have been reported by Celotto *et al* [77]. In addition, it has

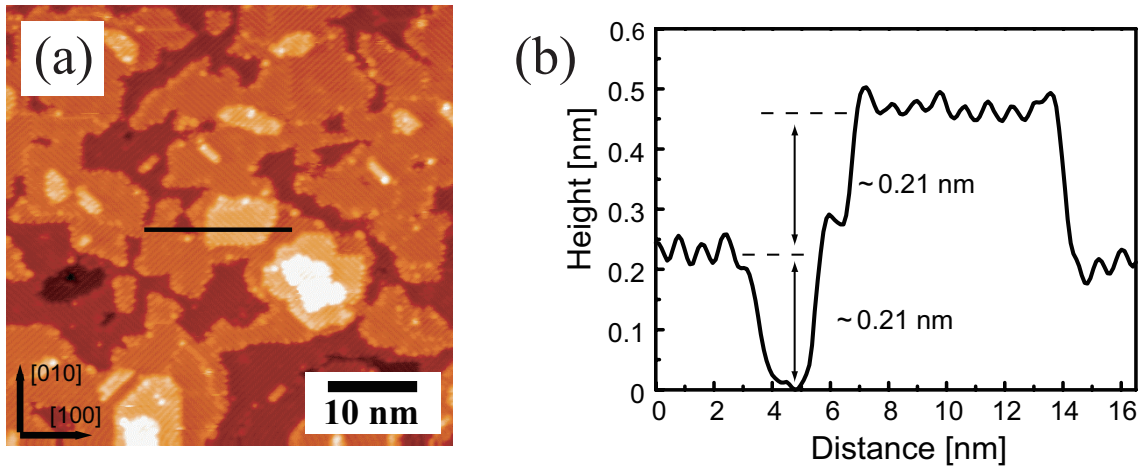


**Figure 7.1** (a) STM image of  $\text{Fe}_3\text{O}_4$  film on  $\text{MgO}(001)$ . The feedback control set point was  $V_S = 2.0$  V,  $I = 1$  nA. The scan size was  $50 \times 50$  nm<sup>2</sup>. Atomically flat terraces exhibiting atomic rows oriented along the [110] direction can be seen. (b) Line profile taken along the black line in the STM image. The step height of  $\sim 0.21$  nm is indicated.

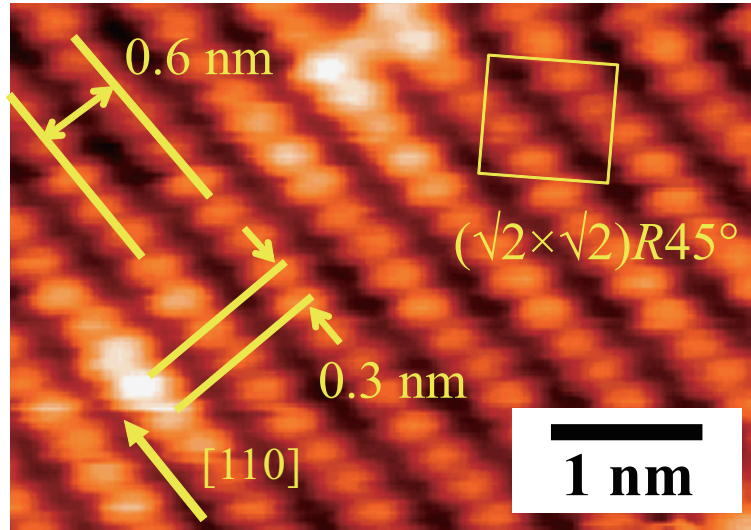


**Figure 7.2** High-resolution STM image of  $\text{Fe}_3\text{O}_4$  film on  $\text{MgO}(001)$ . The feedback control set point was  $V_S = 2.0$  V,  $I = 1$  nA. The scan width was 5 nm. The  $(\sqrt{2} \times \sqrt{2})R45^\circ$  reconstruction unit cell is indicated by the yellow square.

been observed that the surface structure of  $\text{Fe}_\text{B}$  is not significantly different from the structure of  $\text{Fe}_\text{B}$  in the bulk [13, 32, 80]. Thus, we based the surface structure models of the APBs on the bulk configuration.

### 7.2.1 in-plane $1/4[110]$ shift

A topographic image of an APB observed on the surface of an epitaxial grown  $\text{Fe}_3\text{O}_4$  film is shown in Fig. 7.3(a). Two domains are coreless and the APB has formed in between them, as indicated by a dashed line. As shown in this figure, APBs are observed as regions where the periodicity of the corrugation in the image is disrupted. According to the above assumption in which bright corrugation should be assigned to the location of the topmost  $\text{Fe}_\text{B}$  cations, the atomic arrangement of this surface could be represented by a model shown in Fig. 7.3(b). In this drawing, the topmost layer on the surface and the second layer in the subsurface are shown. Oxygen anions are represented by large circles. Lighter circles (red online) indicate Fe cations in octahedral sites (B sites) on the topmost (001) surface and darker ones (blue online) are Fe cations in tetrahedral sites (A sites) located in the second layer. Around these lighter circles, topography observed by STM should be imaged as brighter regions. In the STM image shown in Fig. 7.3(a), single  $\text{Fe}_\text{B}$  sites are not resolved owing to the tip condition; however, bright rows running in the  $[1\bar{1}0]$  direction are observed. The distance between two  $\text{Fe}_\text{B}$  rows on each domain is  $\sim 0.6$  nm as indicated by black lines in Fig. 7.3(a) and 7.3(b). On the other hand, the distance between two  $\text{Fe}_\text{B}$  rows separated by the APB (indicated by gray lines, red online) is  $\sim 0.9$  nm. These features are explained using the APB with a  $1/4[110]$  shift vector. As shown in Fig. 7.3(b), two domains indicated by hatched areas are grown on the surface with a different phase of the periodicity characterized by the shift vector of  $1/4[110]$ . In the left bottom of this figure, a unit cell is marked to explain the origin of periodicity in the domains.

Since there are four types of B-plane in which  $\text{Fe}_\text{B}$  cations are aligned in two different directions with two different phases as shown in Fig. 5.1(b), the APBs with

the  $1/4[110]$  shift vector emerge on the surface in four different ways. By seeking several areas of the surface, two other means of the emergence have been found. Figure 7.4(a) shows an APB that divides domains. The domains have the topmost Fe cations aligned along the  $[1\bar{1}0]$  direction as in the image shown in Fig. 7.3(a). The detailed structure of the APB is vague in the STM image, and it is not clear whether contaminants or instability of the structure causes this ambiguous image. However, the distance between two  $\text{Fe}_B$  rows separated by the APB is thought to be  $\sim 1.5$  nm, and the atomic arrangement of the surface is shown in Fig. 7.4(b). The difference between Figs. 7.3(b) and 7.4(b) is due to the translational relations of the  $\text{Fe}_B$  rows observed in B-planes (4) and (2), as indicated in Fig. 5.1(b). For convenience, two proximate  $\text{Fe}_B$  cations are depicted in the region of the APB. However, it is difficult to discuss the atomic arrangement on the basis of this experimental result.

Figure 7.5(a) also shows an STM image of the APB characterized by the in-plane shift vector of  $1/4[110]$ .  $\text{Fe}_B$  rows running in the  $[110]$  direction are divided by the APB. The APB is observed as a darker valley. The  $\text{Fe}_B$  cations beside the APB are imaged as slightly brighter spots, and the distance between the spots over the APB is  $\sim 0.6$  nm. It should be considered that the observed APB is in B-plane (1) or (3), as shown in Fig. 7.5(b) or 7.5(c). The main difference between the models depicted in these figures is in the periodicity of the  $\text{Fe}_A$  cations. More detailed study of electronic states around the APB should be required to identify which model is preferable to understand the obtained STM image.

As discussed above, our experimental results indicate that the APBs with the in-plane  $1/4[110]$  shift are observed in at least three different ways. This depends on which B-plane is exposed at the surface. According to the crystallographic structure of  $\text{Fe}_3\text{O}_4$ , four different ways are observed for the APBs with the  $1/4[110]$  shift.

### 7.2.2 in-plane $1/2[100]$ shift

An STM image of an APB described by an in-plane shift vector of  $1/2[100]$  is shown in Fig. 7.6(a). As discussed in the previous section, four different types of B-planes should be considered. However, two of them form equivalent atomic arrangements because of the symmetry of the APB. That is, APBs in B-planes (1) and (3) or B-planes (2) and (4) have the same atomic pattern. In this STM image, bright rows corresponding to  $\text{Fe}_B$  cation rows run in the  $[110]$  direction; they shift by  $\sim 0.3$  nm at the APB. This APB is a region where two domains shifted by  $1/2[100]$  coalesce, as shown in 7.6(b). The atomic structure around the APB is not resolved in the STM image, and it is difficult to identify locations of  $\text{Fe}_B$  cations on the APB, as shown in Fig. 7.6(b). The  $\text{Fe}_B$  cations in the region of the APB shown in this figure are depicted for convenience to understand the direction of the shift vector, and they do not necessarily indicate the actual locations of the cations. This type of APB was seldom observed in our STM measurements. In our STM images, the portion of the APBs recognized into this type was about 1%.

### 7.2.3 out-of-plane $1/4[101]$ shift

The most frequently observed APBs are those with an out-of-plane shift vector of  $1/4[101]$ . The STM image shown in Fig. 7.7(a) suggests that the observed APB should be classified into this type of APB.  $\text{Fe}_B$  rows are rotated by  $90^\circ$  at the APB with respect to the  $\text{Fe}_B$  rows in the neighboring domain. Because of the symmetry of B-planes containing this type of APB, two possible atomic arrangements are provided at the surface. The topographic image of this APB makes it possible to assign its atomic arrangements into one of the models of the surface, as shown in Fig. 7.7(b). In contrast to the previous STM images, the surface structure around the APB is clear. Bright spots observed on the APB could be assigned to  $\text{Fe}_B$  cations at the center of the APB, as depicted in Fig. 7.7(b).

Since the atomic configurations of APBs surrounding an antiphase domain are

not simple, several types of boundaries consisting of the fundamental APBs that have been discussed so far are observed, as shown in Fig. 7.7(c). In this image, an APB running along the  $[130]$  direction is observed. Carefully looking into the topographic image of the boundary, it can be recognized that this boundary consists of APBs characterized by the out-of-plane shift vector of  $1/4[101]$ . Investigating several STM images taken on four different  $\text{Fe}_3\text{O}_4$  films that were grown under the same experimental conditions, about 61% of identified APBs are categorized into the APB with this type of the shift vector.

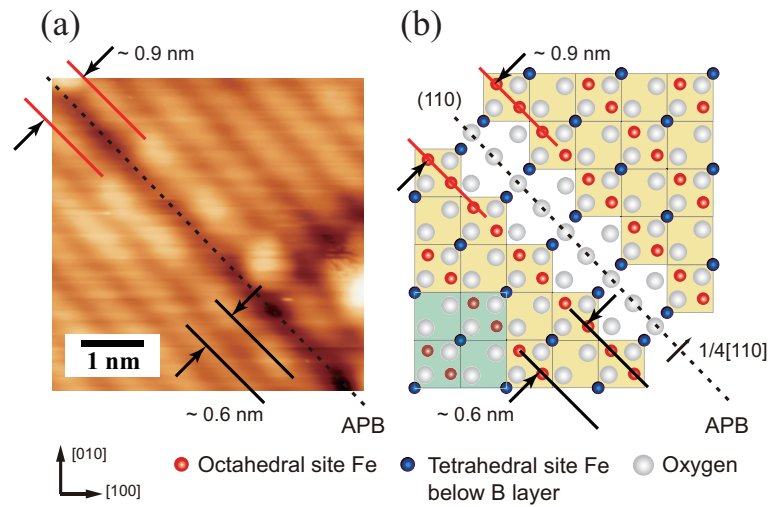


**Figure 7.3** (a) STM image of an APB with a  $1/4[110]$  shift. The feedback control set point was  $V_S = 2.0$  V,  $I = 0.3$  nA. The scan size was  $5 \times 5$  nm<sup>2</sup>. The APB is in a (110) plane. (b) Possible surface atomic configuration around an APB with a  $1/4[110]$  shift.

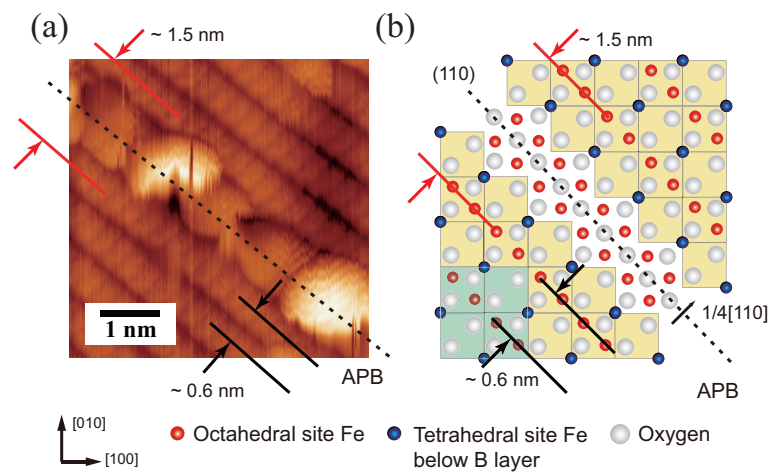


**Figure 7.4** (a) STM image of an APB which has a  $1/4[110]$  shift. The feedback control set point was  $V_S = 1.5$  V,  $I = 0.7$  nA. The scan size was  $5 \times 5$  nm<sup>2</sup>. (b) Possible surface atomic configuration around an APB with a  $1/4[110]$  shift.

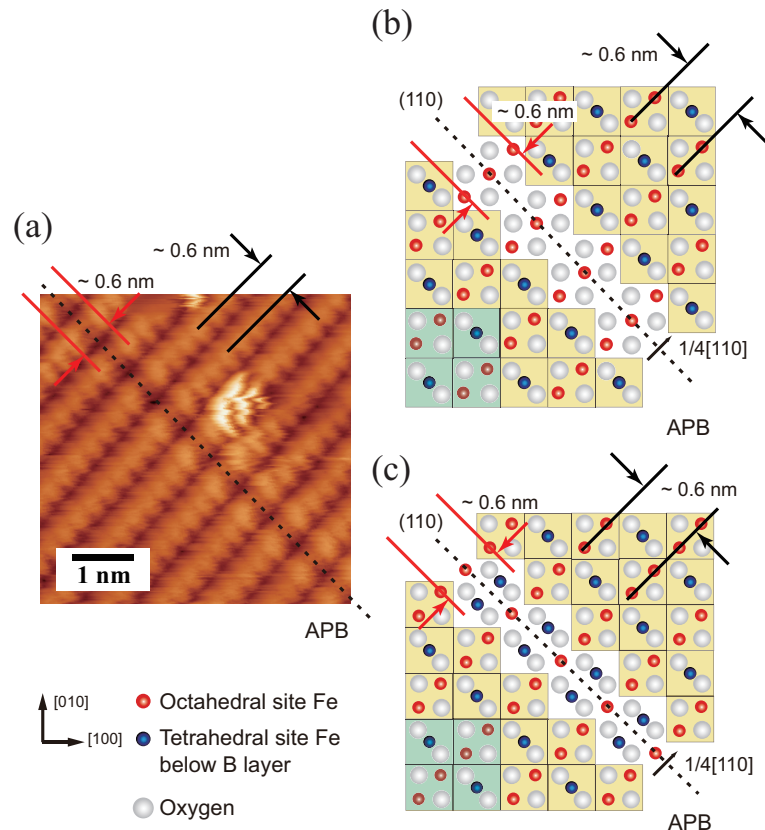


**Figure 7.5** (a) STM image of an APB with a  $1/4[110]$  shift. The feedback control set point was  $V_S = 1.5$  V,  $I = 0.8$  nA. The scan size was  $5 \times 5$  nm<sup>2</sup>. (b) and (c) Possible surface atomic configuration around an APB with a  $1/4[110]$  shift.

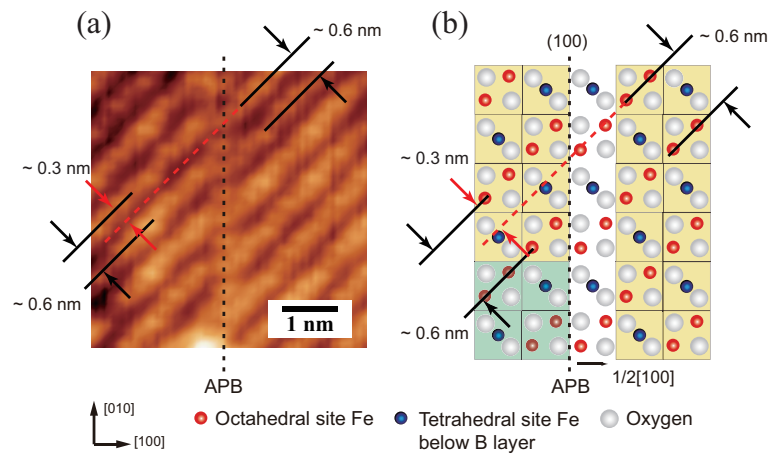


**Figure 7.6** (a) STM image of an APB with a  $1/2[100]$  shift. The feedback control set point was  $V_S = 1.6$  V,  $I = 1$  nA. The scan size was  $5 \times 5$  nm<sup>2</sup>. The APB is in a (100) plane. (b) Possible surface atomic configuration around an APB with a  $1/2[100]$  shift.

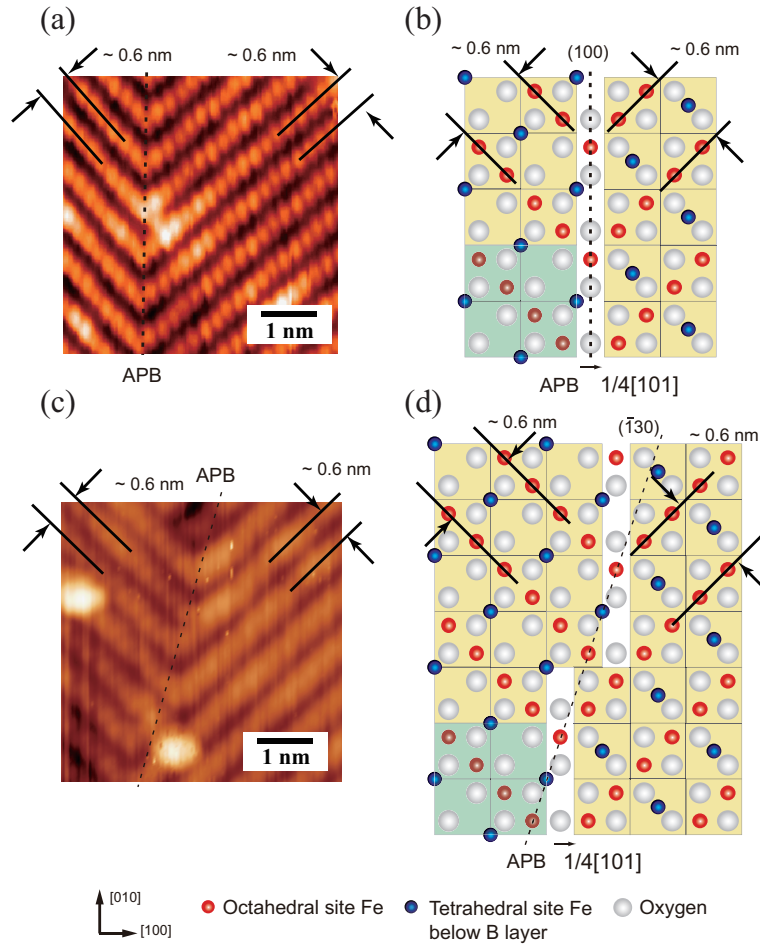


**Figure 7.7** (a) STM image of an APB with a  $1/4[101]$  shift. The feedback control set point was  $V_S = 2.0$  V,  $I = 1$  nA. The scan size was  $5 \times 5$  nm<sup>2</sup>. The APB is in a (100) plane. (b) Possible surface atomic configuration around an APB with a  $1/4[101]$  shift and a (110) boundary plane. (c) STM image of an APB with a  $1/4[101]$  shift. The feedback control set point was  $V_S = 2.0$  V,  $I = 0.3$  nA. The scan size was  $5 \times 5$  nm<sup>2</sup>. The APB is in a  $(\bar{1}30)$  plane. (d) Possible surface atomic configuration around an APB with a  $1/4[101]$  shift and a  $(\bar{1}30)$  boundary plane.

### 7.3 Observation of spin-polarized surface states on a $\text{Fe}_3\text{O}_4$ film by SP-STS

In this section, we discuss spin-polarized surface states on  $\text{Fe}_3\text{O}_4$  films that includes out-of-plane type APB. A STM image of the topography and a corresponding  $dI/dV$  map at a bias voltage of 1.2 V, are shown in Fig.7.8(a) and 7.8(b), respectively. Both of the images were simultaneously obtained on the same area. The out-of-plane type APB is clearly observed in Fig. 7.8(a). Figure 7.8(c) and 7.8(d) are histograms of  $dI/dV$  signal intensity derived from the area indicated by black solid and dashed rectangles in Fig. 7.8(b), respectively. These are adsorbent and defect free areas. Gaussian fits were used to determine the average  $dI/dV$  values. Let  $I_{Left,Right}$  be the averaged intensity of the  $dI/dV$ -signal measured at the left (right) domain which separated by the APB, then we find  $I_{Left} = 5.155 \pm 0.004$  and  $I_{Right} = 5.449 \pm 0.003$ .  $I_{Left}$  is lower than  $I_{Right}$ . To quantitatively compare with these data, we consider an asymmetry parameter

$$A = \left| \frac{I_{Left} - I_{Right}}{I_{Left} + I_{Right}} \right|. \quad (7.1)$$

These values result in the  $A$  at  $V_{sample} = 1.2$  V of  $A = (3.23 \pm 0.05)\%$ .

As a reference, we also conducted STS measurement on the same  $\text{Fe}_3\text{O}_4$  film that includes out-of-plane type APB with nonmagnetic W tip. A STM image of the topography and a corresponding  $dI/dV$  map at a bias voltage of 1.2 V, are shown in Fig.7.9(a) and 7.9(b), respectively. The same type APB shown in Fig. 7.8(a) is clearly observed in Fig. 7.9(a). Figure 7.9(c) and 7.9(d) are histograms of  $dI/dV$  signal intensity derived from the area indicated by black solid and dashed rectangles in Fig. 7.9(b), respectively. We calculated the  $I_{Left}$ ,  $I_{Right}$  and  $A$  similarly as above, then we find  $I_{Left} = 2.128 \pm 0.003$ ,  $I_{Right} = 2.099 \pm 0.002$ , and  $A = (0.68 \pm 0.08)\%$ . It indicate that the average value of the electronic states of left and right domain separated by the out-of-plane type APB are virtually equivalent.

In the case of SP-STS measurement with spin-polarized Cr/W tip, the  $A$  is much than that of STS measurement with nonmagnetic W tip and has the non-zero value.

It can be said that the spin-polarized surface states were observed on  $\text{Fe}_3\text{O}_4$  film. The higher (lower) average  $dI/dV$  value means that the direction on the magnetization of the  $\text{Fe}_B$  on the right (left) domain is parallel (anti-parallel) to that of the apex of the spin-polarized Cr/W tip. Therefore, it can be said that the out-of-plane type APB induces antiferromagnetic coupling between adjacent domains.

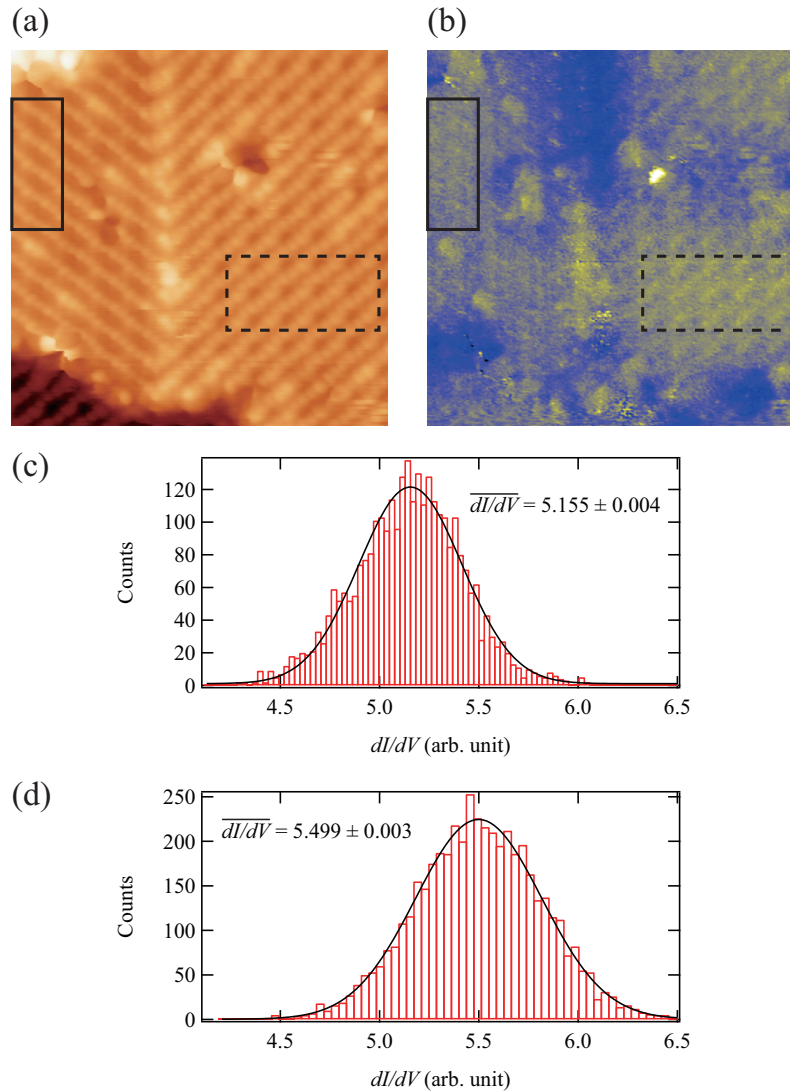


**Figure 7.8** (a)  $(10 \times 10)$  nm<sup>2</sup> STM image of the topography. The image of the  $\text{Fe}_3\text{O}_4(001)$  film was taken with Cr/W-tip at a tunneling current of 0.3 nA and a bias voltage of 1.2 V. (b)  $dI/dV$  map at a bias voltage of 1.2 V for the same region shown in (a). (c) Histograms of  $dI/dV$  signal intensity derived from the area indicated by black solid rectangles in Fig. 7.8(b). (d) Histograms of  $dI/dV$  signal intensity derived from the area indicated by black dashed rectangles in Fig. 7.8(b)

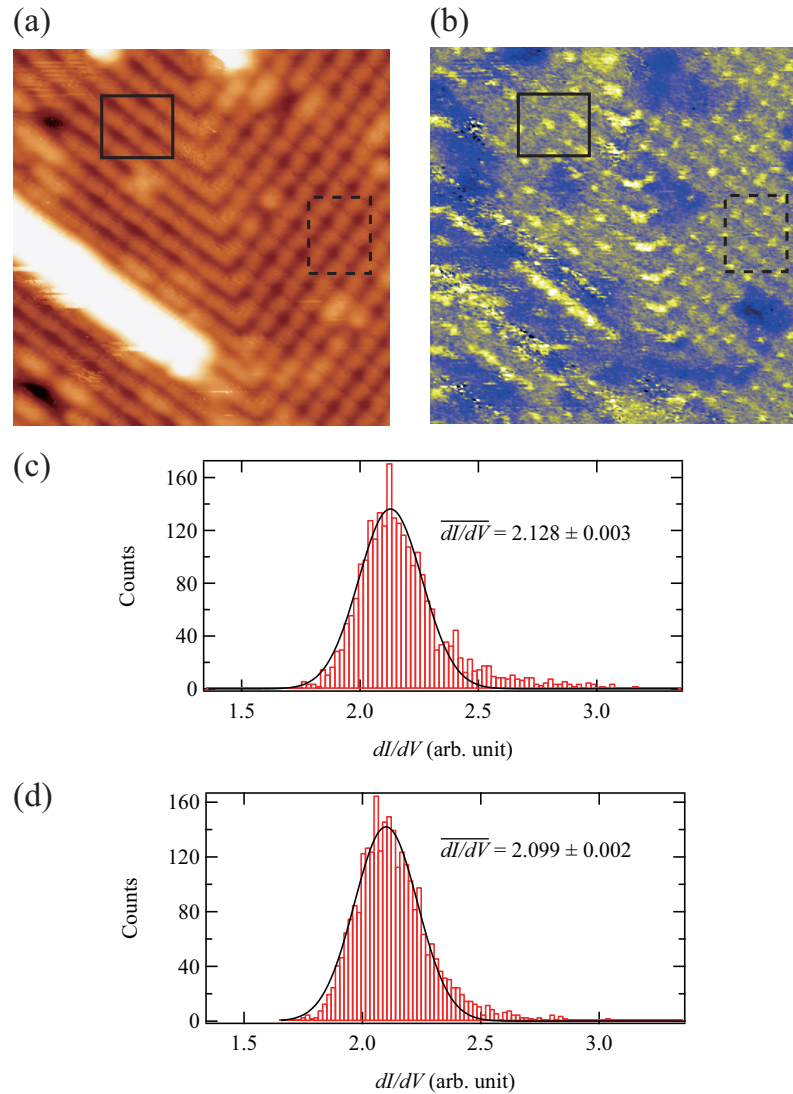


**Figure 7.9** a)  $(10 \times 10) \text{ nm}^2$  STM image of the topography. The image of the  $\text{Fe}_3\text{O}_4(001)$  film was taken with Cr/W-tip at a tunneling current of 0.3 nA and a bias voltage of 1.2 V. (b)  $dI/dV$  map at a bias voltage of 1.2 V for the same region shown in (a). (c) Histograms of  $dI/dV$  signal intensity derived from the area indicated by black solid rectangles in Fig. 7.9(b). (d) Histograms of  $dI/dV$  signal intensity derived from the area indicated by black dashed rectangles in Fig. 7.9(b)

# Chapter 8

## Summary

In this part, we have revealed how APBs are observed on the surfaces of  $\text{Fe}_3\text{O}_4$  films grown epitaxially on  $\text{MgO}(001)$  substrates. By comparing simple models of APBs, the observed APBs in our experiment are categorized into boundaries with three different phase shift vectors. A reduction in the symmetry of the surface caused by the introduction of APBs gives the surface structures of APBs some variations. The observed APBs in our experiment are classified under the APBs that have been observed by Celotto *et al.* with transmission electron microscopy (TEM) [77]. The tendency of the proportions of each type of APB estimated using our experimental results (48 images of 8 samples) are nearly the same as that in their report [77]. In our experiment, the proportion of the APBs with an in-plane  $1/4[110]$  shift is about 38% and that of the APBs with an out-of-plane  $1/4[101]$  shift is about 61%. Only about 1% of the boundaries are classified into APBs with an in-plane  $1/2[100]$  shift. We have also conducted SP-STs measurement on the  $\text{Fe}_3\text{O}_4$  film which include the out-of-plane type APB. Different average  $dI/dV$  values were measured between two domains separated by the out-of-plane type APB. An asymmetry parameter  $A = (3.23 \pm 0.05)\%$ , which means that the out-of-plane type APB induces antiferromagnetic coupling between adjacent domains.. These findings discussed in this thesis will be useful for the investigation of local electronic properties or magnetic properties in regions containing well-defined APBs.

## Part III

# Surface and subsurface electronic structures in $\text{Fe}_3\text{O}_4$ films on $\text{MgO}(001)$



# Abstract

We have performed scanning tunneling microscopy/spectroscopy (STM/STS) on  $\text{Fe}_3\text{O}_4(001)$  films. The sample consisted of 20 nm thick epitaxial films were grown by molecular beam epitaxy (MBE) on  $\text{MgO}(001)$  substrates. On the surface of the films, individual iron atoms and surface  $(\sqrt{2} \times \sqrt{2})R45^\circ$  reconstruction are clearly observed by STM. In STS study, we have taken differential conductance ( $dI/dV$ ) maps. A charge ordered electronic structures are observed in a  $dI/dV$  map. The structures is similar to that of the model of the charge ordering of  $\text{Fe}^{2+}\text{-Fe}^{2+}$  and  $\text{Fe}^{3+}\text{-Fe}^{3+}$  dimer in the layer beneath the top layer proposed by density functional theory (DFT) studies. STS measurements also reveal that DOS of surface octahedral iron ( $\text{Fe}_B$ ) has an energy gap of about 0.7 V, and the valence of the surface  $\text{Fe}_B$  atoms should be close to  $\text{Fe}^{3+}$ .

# Chapter 9

## Introduction

The  $\text{Fe}_3\text{O}_4(001)$  surface structure has been studied by scanning tunneling microscopy/spectroscopy (STM/STS) and Low energy electron diffraction (LEED), and a  $(\sqrt{2} \times \sqrt{2})R45^\circ$  surface reconstruction have been often observed on the  $\text{Fe}_3\text{O}_4(001)$  surface. Several groups have observed individual  $\text{Fe}_B$  in B-plane by STM, which shows a wavelike structure of the iron rows running along the  $[110]$  direction (see Fig. 9.1(a)) [12, 32, 37, 40, 80]. Emergence of the B-terminated surface structure has been also predicted by density functional theory (DFT) using the generalized gradient approximation (GGA) calculations performed by Pentcheva *et al.* [4, 6]. They suggested that the  $(\sqrt{2} \times \sqrt{2})R45^\circ$  reconstruction is a result of a Jahn-Teller distortion and the surface is metallic. However, the STS study by Jordan *et al.* has reported that the surface band gap of  $\sim 0.2$  eV is present which means that the surface is insulative. On the other hand, DFT (GGA+U) calculations have been proposed that the charge states of the  $\text{Fe}_B$  ions beneath the surface is ordering, the subsurface charge ordering causes a  $(\sqrt{2} \times \sqrt{2})R45^\circ$  surface reconstruction, and a  $\sim 0.3$  eV band gap exists. [5, 85]. Figure 9.1(b) is the sketch of the proposed subsurface charge ordering structure. The  $\text{Fe}^{2+}$ - $\text{Fe}^{2+}$  and  $\text{Fe}^{3+}$ - $\text{Fe}^{3+}$  dimers line up along  $[1\bar{1}0]$  alternately in the subsurface layer, and surface is terminated with  $\text{Fe}^{3+}$  cations. In the surface layer, the displacement of the  $\text{Fe}^{3+}$  cations produce inequivalent narrow “n” and wide “w” sections. The inequivalent sections compose the  $(\sqrt{2} \times \sqrt{2})R45^\circ$  surface reconstruction pattern. In addition, they have also predicted that the surface is terminated by  $\text{Fe}^{3+}$  cations. We have to note that, in this thesis, we labeled two charge states of the  $\text{Fe}_B$  ions as  $\text{Fe}^{2+}$  and  $\text{Fe}^{3+}$ , although the valence charge of the cations is larger than the other by  $(0.2-0.4)e$  [5]. This subsurface charge ordering model has been

supported by DFT using the projector augmented waves (PAW) calculations [7]. On the other hand, surface charge ordering structure have been observed by several groups. A magnetic structure of  $\text{Fe}_3\text{O}_4(001)$  by using a ferromagnetic Fe-tip [86–88]. These studies has suggested that a charge ordering of  $\text{Fe}^{2+}$  and  $\text{Fe}^{3+}$  cations exists at the surface at room temperature. More recently, another surface charge ordering structure which consists of  $\text{Fe}^{2+}\text{-Fe}^{2+}$  and  $\text{Fe}^{3+}\text{-Fe}^{3+}$  dimers, has been reported by spin-polarized STM (SP-STM) studies with an antiferromagnetic MnNi-tip [34, 36] and a ferromagnetic Ni-tip [13, 37]. However, while SP-STM has clearly observed the dimers, individual surface irons has not been resolved. Therefore, the surface and subsurface charge states of  $\text{Fe}_B$  ions remain unclear.

The aim of this part is to reveal surface atomic and electronic structure. We have performed STM and STS on  $\text{Fe}_3\text{O}_4(001)$  films using an antiferromagnetic Cr (or ferromagnetic Fe) coated W-tip (Cr/W-tip or Fe/W-tip), in order to reveal surface atomic and electronic structure. The  $(\sqrt{2} \times \sqrt{2})R45^\circ$  reconstructed B-terminated surface structure is observed by STM with true atomic resolution (i.e., imaging of individual surface irons). In STS measurements, subsurface charge ordering structures similarly reported in DFT (GGA+U) and DFT (PAW) studies [5, 7] are observed in differential tunneling conductance ( $dI/dV$ ) map.

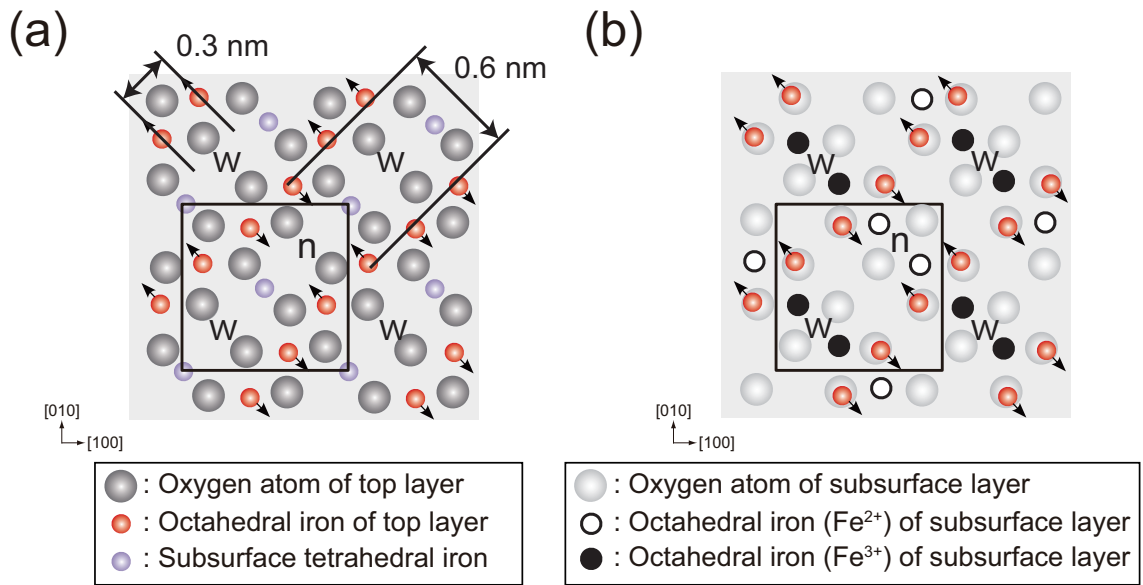


**Figure 9.1** (a) Model of the B-terminated surface structure of  $\text{Fe}_3\text{O}_4(001)$  proposed by Pentcheva et al [4–6]. The black arrows indicate the directions of the displacements of octahedral irons. The narrow and wide section are marked as “n” and “w”. (b) Model of the subsurface charge ordering structure with a  $(\sqrt{2} \times \sqrt{2})R45^\circ$  reconstructed unit cell. The  $(\sqrt{2} \times \sqrt{2})R45^\circ$  cell is indicated by a black square.

# Chapter 10

## Experimental

The experiments were carried out in the same conditions as describe in Cap. 6.

The epitaxially grown  $\text{Fe}_3\text{O}_4(001)$  thin films were prepared on cleaved  $\text{MgO}(001)$  single-crystal substrates by the deposition of Fe in the presence of oxygen. The  $\text{MgO}(001)$  substrates were cleaned *in situ* by heating at 573 K over 12 hours and then annealed at 1073 K for 1 hour in oxygen atmosphere ( $7 \times 10^{-7}$  mbar). The Fe deposition were performed using an electron-beam heating evaporator (Omicron EFM 3) at a substrate temperature of 573 K. During the film formation, the oxygen pressure was set in the range from  $7 \times 10^{-7}$  to  $1 \times 10^{-6}$  mbar. The growth rate was 0.9 ML/min and the film thickness was 20 nm [12, 13, 37, 40]. After the deposition, the grown films were annealed at 573 K for 30 min in the same oxygen atmosphere.

# Chapter 11

## Results and Discussion

### 11.1 Subsurface charge ordering

Figure 11.1 is an constant current STM image of the  $\text{Fe}_3\text{O}_4(001)$  film surface grown on the  $\text{MgO}(001)$  substrate. The STM image was taken at a tunneling current of 0.3 nA and a bias voltage of 1.2 V. In Fig. 11.1(a), atomic rows with the  $(\sqrt{2} \times \sqrt{2})R45^\circ$  symmetry (marked with a white square in Fig. 11.1) running along  $[110]$  direction are clearly resolved. As can be seen in a line profile indicating as the line “A” in Fig. 11.1(b), the averaged distance between neighboring rows is about 0.6 nm. The STM image and the line profile “A” also revealed that the bright spots within each row are slightly shifted along the directions perpendicular to the rows. It clearly shows that the narrow and wide section shown in Fig. 9.1 are exist. Within the rows, the difference of the height between next neighbor atoms is observed and the distance between the atoms is about 0.3 nm (see line profile “B” in Fig. 11.1(b)). These small displacements of the atoms perpendicular to the rows and the (001) plane have been reported by DFT calculations and low energy electron diffraction (LEED) analysis [6]. Since the periodicities and the shifts of the bright spots are correspond to those of  $\text{Fe}_B$  ions in the surface structure model of B-terminated  $\text{Fe}_3\text{O}_4(001)$  (shown in Fig. 9.1(a)), each bright spots in Fig. 11.1(a) should represent single  $\text{Fe}_B$  ions in the B-plane.

We performed  $dI/dV$  mapping on the  $\text{Fe}_3\text{O}_4(001)$  films in order to explore the surface electronic structures of the films. A STM image of the topography and a corresponding  $dI/dV$  map at a bias voltage of 1.2 V, are shown in Fig.11.2(a)

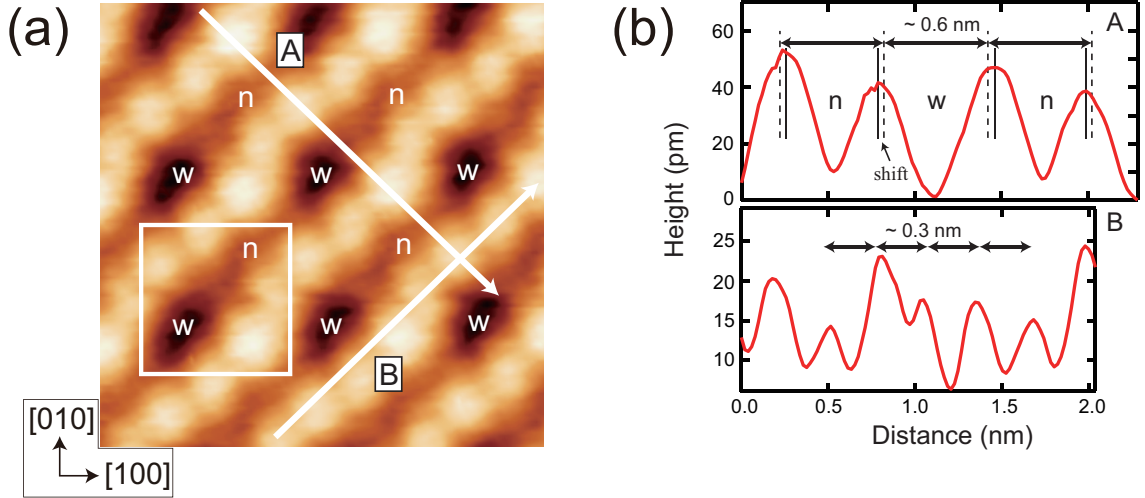


**Figure 11.1** (a)  $(2.5 \times 2.5)$  nm<sup>2</sup> STM image of the  $\text{Fe}_3\text{O}_4(001)$  film. The image was taken with Cr/W-tip at a tunneling current of 0.3 nA and a bias voltage of 1.2 V. The  $(\sqrt{2} \times \sqrt{2})R45^\circ$  reconstruction unit cell is indicated by the white square. The narrow and wide section are marked as “n” and “w”. Individual  $\text{Fe}_B$  ions are imaged. (b) Line profiles taken along  $[1\bar{1}0]$  and  $[110]$  directions marked as “A” and “B” in (a).

and 11.2(b), respectively. Both of the images were simultaneously obtained on the same area. Fig.11.2(c) shows cross sectional line profiles of the topography and the  $dI/dV$  map taken along the arrows marked as “C” and “D”. The relative positions of the arrows are same. In Fig.11.2(a), the B-terminated  $\text{Fe}_3\text{O}_4(001)$  surface with individual  $\text{Fe}_B$  atoms are clearly observed, and iron rows are running along  $[110]$  direction. Meanwhile, the  $dI/dV$  map shows a periodic structure different from that in the STM image. It is composed of two different  $dI/dV$  signal intensity (“high-peak” and “low-peak”) as indicated by the line profile “D” shown in Fig. 11.2(c). The line profile is taken along the  $[1\bar{1}0]$  direction (i.e., the perpendicular direction to iron rows), and indicates a  $\sim 0.6$  nm periodicity. The periodicities of high(low)-peak to high(low)-peak are  $\sim 1.2$  nm. In the  $dI/dV$  map, these periodic structure shows a  $(\sqrt{2} \times \sqrt{2})R45^\circ$  symmetry as indicated with a white square in Fig. 11.2(b). By comparing the positions of bright spots in  $dI/dV$  map with surface atomic structure,

it is found that the bright spots locate between  $\text{Fe}_B$  rows (see in Fig.11.2(a) and (b)). In Fig.11.2(c), it can be seen that the positions of high(low)-peaks are correspond to that of wide(narrow) sections. Therefore, it is possible that the origin of the peaks is the electronic states of surface oxygen atom or  $\text{Fe}_B$  atom in subsurface layer (see in Fig.9.1). According to the DOS calculation by Bernal *et al.*, it has predicted that the DOS of subsurface  $\text{Fe}^{3+}$  is higher than that of subsurface  $\text{Fe}^{2+}$ , and the DOS of surface oxygen is almost zero at the energy level of 1.2 eV (see, in particular, Fig.6(b) in Section 4 of Ref. [7]). Consequently, the “high(low)-peak” should represent the existence of the dimer of  $\text{Fe}^{3+}\text{-Fe}^{3+}$  ( $\text{Fe}^{2+}\text{-Fe}^{2+}$ ) in subsurface layer.

We also performed STS measurements on the  $\text{Fe}_3\text{O}_4(001)$  films. The spectra were taken on four different surface  $\text{Fe}_B$  sites. Figure11.4(a) shows the STM image and the locations of the STM tip where STS spectra were collected. These locations are indicated by a red circle( $\circ$ ), blue cross( $\times$ ), green triangle ( $\triangle$ ) and black cross( $+$ ). At these locations, the tip is located above  $\text{Fe}_B$  sites. Figure 11.4(b) shows the normalized tunneling conductance  $(dI/dV)/(\overline{I/V})$  curves taken at these locations. The curves were converted from the  $I(V)$  data using the procedure developed by Feenstra *et al.* [8]. The  $I(V)$  data was obtained for tunneling set points of +1 V and 0.2 nA. As can be seen in Fig.11.4(b), a band gap value of about 0.7 eV is obtained in all  $(dI/dV)/(\overline{I/V})$  curves, and the gap is opening from  $-0.7$  to 0 V. The band gap value of 0.7 eV is larger than that of 0.2 V which has been reported by Jordan *et al.* [89]. They obtained the value by averaging  $I(V)$  data taken from a specific area on the  $\text{Fe}_3\text{O}_4(001)$  surface, thus it includes the properties of not only the  $\text{Fe}_B$  atoms but also other surface area. Indeed, we also obtained smaller values than 0.2 eV at the locations near a step edge and an adsorbate site such as an OH-group on the  $\text{Fe}_3\text{O}_4(001)$  surface. Meanwhile, our  $(dI/dV)/(\overline{I/V})$  curves were taken above the  $\text{Fe}_B$  sites. To the knowledge of the authors, the data as shown in Fig.11.4(b) for individual  $\text{Fe}_B$  atom has not been reported so far. Moreover, these features of  $\sim 0.7$  eV band gap and the gap region from  $-0.7$  to 0 V, are similar to that of the DOS of surface  $\text{Fe}_B$  atom at room temperature calculated by the DFT (PAW) method (see Fig. 11.3(c)) [7]. From these result, the valence of the  $\text{Fe}_B$  in the  $\text{Fe}_3\text{O}_4(001)$

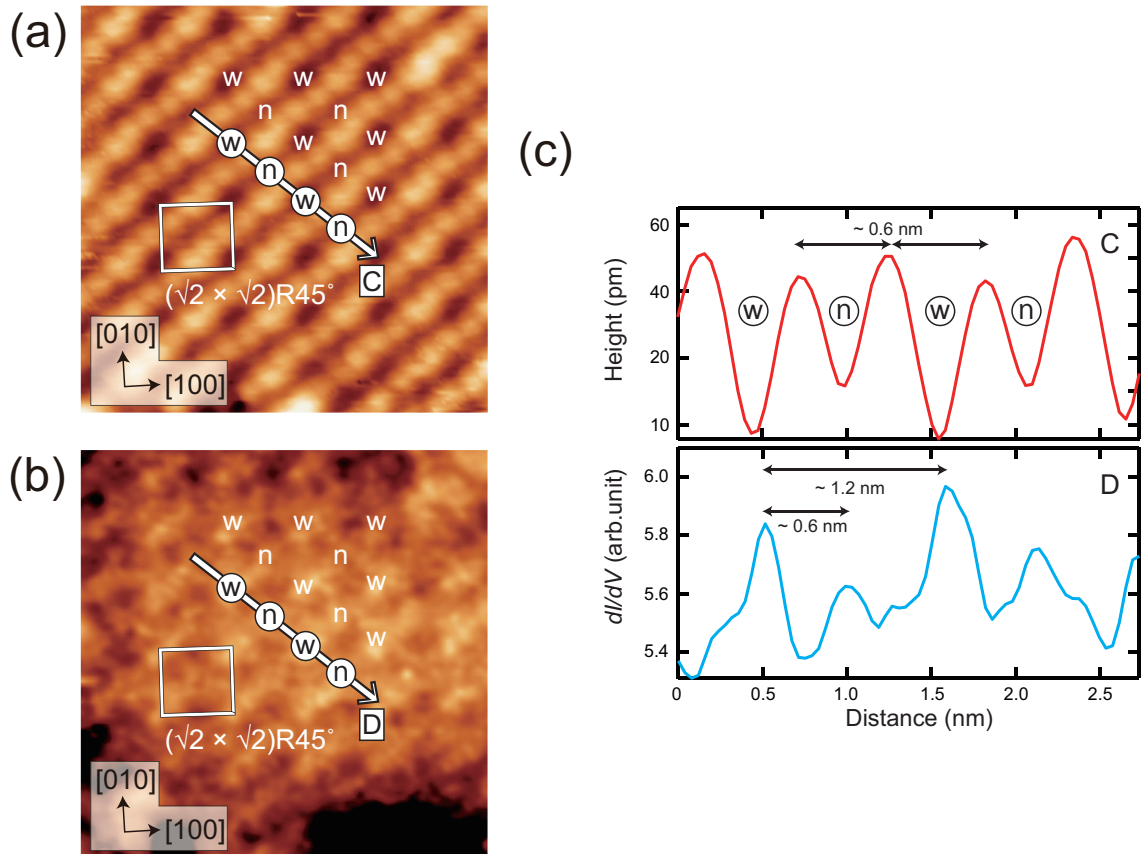


**Figure 11.2** (a)  $(4.7 \times 4.7)$  nm<sup>2</sup> STM image of the topography. The image of the Fe<sub>3</sub>O<sub>4</sub>(001) film was taken with Cr/W-tip at a tunneling current of 0.3 nA and a bias voltage of 1.2 V. The dashed line indicates an APB. (b)  $dI/dV$  map at a bias voltage of 1.2 V for the same region shown in (a). The white open rectangle indicates the  $(\sqrt{2} \times \sqrt{2})R45^\circ$  reconstruction unit cell. The narrow and wide section are marked as “n” and “w”. (c) Line profiles of the topography and the  $dI/dV$  signal taken along the arrows marked as “C” and “D” in (a) and (b), respectively. The relative position of the arrows is same.

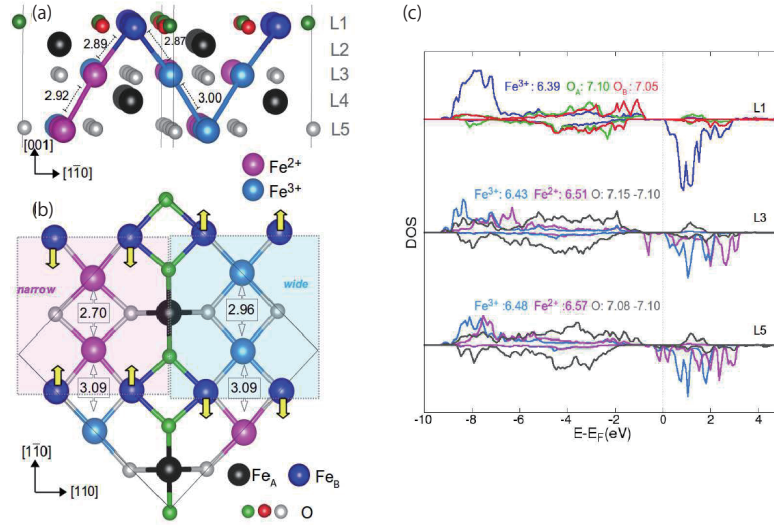


**Figure 11.3** (a) Top and (b) side views of the  $\text{Fe}_3\text{O}_4(001)$  surface. Panel (b) only shows the 3 outermost planes, indicating the different in-plane  $\text{Fe}_B\text{-Fe}_B$  distance in Å. (c) Spin-resolved DOS of all inequivalent atoms (blue for Fe, red/green for surface O) at the outermost B-plane. [7]

surface layer should be confirmed to be  $\text{Fe}^{3+}$ , and this charge freezing at the surface can cause the surface Verwey transition.

As we discussed above, we observed subsurface charge ordering like electronic structure composed of  $\text{Fe}^{3+}\text{-Fe}^{3+}$  and  $\text{Fe}^{2+}\text{-Fe}^{2+}$  dimers, and measured surface  $\text{Fe}_B$  electronic property which shows the band gap value of  $\sim 0.7$  eV. By combining our results with the DFT studies, we found that the surface of  $\text{Fe}_3\text{O}_4(001)$  are terminated by  $\text{Fe}^{3+}$  cation and subsurface  $\text{Fe}_B$  ions show charge ordering of  $\text{Fe}^{2+}\text{-Fe}^{2+}$  and  $\text{Fe}^{3+}\text{-Fe}^{3+}$ .

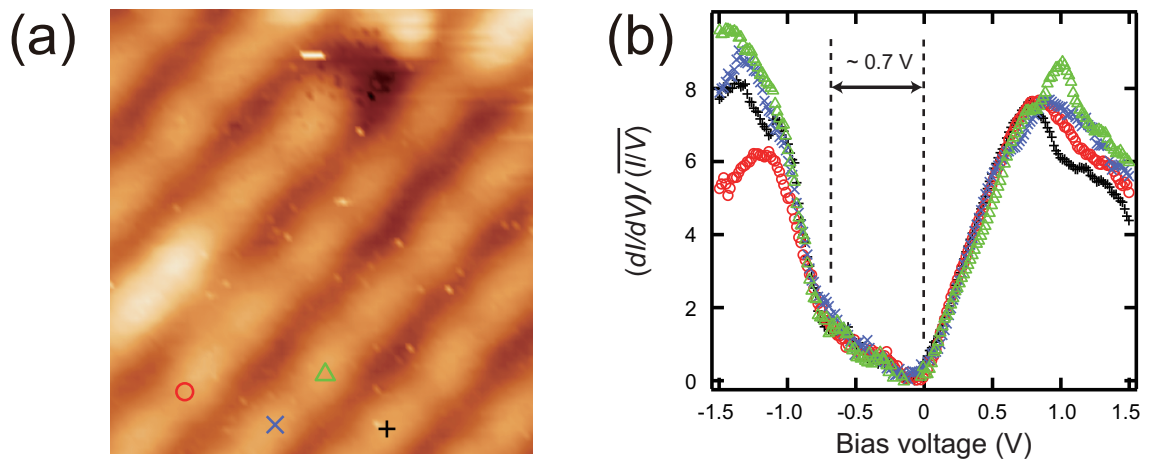


**Figure 11.4** (a)  $(3 \times 3)$  nm<sup>2</sup> STM image of the  $\text{Fe}_3\text{O}_4(001)$  film. The image was taken with Cr/W-tip at a tunneling current of 0.2 nA and a bias voltage of 1.2 V. The locations of STM tip for STS measurements are indicated by red circle(○), blue cross(×), green triangle(△) and black cross(+). (b)  $(dI/dV)/(I/V)$  curves taken on surface  $\text{Fe}_B$  sites. These curves were taken at the corresponding mark and converted from the  $I(V)$  curve using the procedure developed by Feenstra *et al.* [8]

# Chapter 12

## Summary

We have employed STM/STS with the antiferromagnetic Cr/W-tip in order to reveal the surface atomic and electronic structure of the  $\text{Fe}_3\text{O}_4(001)$  films. STM resolved individual  $\text{Fe}_B$  ions and B-terminated surface structure with  $(\sqrt{2} \times \sqrt{2})R45^\circ$  symmetry. The observed surface structure corresponds to the model reported by Pentcheva et al [4–7] and the results of the STM studies with W-tip [12, 32, 37, 40, 80]. Our STS result showed the presence of the charge ordering in the  $\text{Fe}_3\text{O}_4(001)$  subsurface layer. The subsurface charge ordering structure showing an alternation of two types of corrugations, has  $(\sqrt{2} \times \sqrt{2})R45^\circ$  symmetry. It is very similar to the model of subsurface charge ordering [5, 7]. Moreover, STS spectra taken above surface  $\text{Fe}_B$  atoms could be indicative that the surface is terminated by  $\text{Fe}^{3+}$  cations. Our results suggest that the surface of  $\text{Fe}_3\text{O}_4(001)$  are terminated by  $\text{Fe}^{3+}$  cation and subsurface  $\text{Fe}_B$  ions show charge ordering of  $\text{Fe}^{2+}\text{-Fe}^{2+}$  and  $\text{Fe}^{3+}\text{-Fe}^{3+}$ .

# References

- [1] J. Tersoff and D. R. Hamann. “Theory and Application for the Scanning Tunneling Microscope”. *Phys. Rev. Lett.*, Vol. **50**, pp. 1998–2001, (1983).
- [2] J. Tersoff and D. R. Hamann. “Theory of the scanning tunneling microscope”. *Phys. Rev. B*, Vol. **31**, pp. 805–813, (1985).
- [3] Joseph A. Stroscio, D. T. Pierce, A. Davies, and R. J. Celotta. Tunneling spectroscopy of bcc(001) surface states. *Phys. Rev. Lett.*, Vol. 75, p. 2960, 1995.
- [4] R Pentcheva, F Wendler, HL Meyerheim, W Moritz, N Jedrecy, and M Scheffler. Jahn-Teller stabilization of a “polar” metal oxide surface: Fe<sub>3</sub>O<sub>4</sub>(001). *PHYSICAL REVIEW LETTERS*, Vol. 94, No. 12, APR 1 2005.
- [5] Zbigniew Lodziana. Surface verwey transition in magnetite. *PHYSICAL REVIEW LETTERS*, Vol. 99, No. 20, NOV 16 2007.
- [6] R. Pentcheva, W. Moritz, J. Rundgren, S. Frank, D. Schrupp, and M. Scheffler. A combined DFT/LEED-approach for complex oxide surface structure determination: Fe<sub>3</sub>O<sub>4</sub>(001). *SURFACE SCIENCE*, Vol. 602, No. 7, pp. 1299–1305, APR 1 2008.
- [7] Ivan Bernal-Villamil and Silvia Gallego. Charge order at magnetite fe<sub>3</sub>o<sub>4</sub> (0 0 1): surface and verwey phase transitions. *Journal of Physics: Condensed Matter*, Vol. 27, No. 1, p. 012001, 2015.

- 
- [8] R. M. Feenstra. Tunneling spectroscopy of the (110) surface of direct-gap iii-v semiconductors. *Phys. Rev. B*, Vol. 50, pp. 4561–4570, Aug 1994.
- [9] Akira Yanase and Kiiti Siratori. Band structure in the high temperature phase of  $\text{Fe}_3\text{O}_4$ . *Journal of the Physical Society of Japan*, Vol. 53, No. 1, pp. 312–317, 1984.
- [10] Akira Yanase and Noriaki Hamada. Electronic structure in high temperature phase of  $\text{Fe}_3\text{O}_4$ . *Journal of the Physical Society of Japan*, Vol. 68, No. 5, pp. 1607–1613, 1999.
- [11] EJW Verwey. Electronic conduction of magnetite ( $\text{Fe}_3\text{O}_4$ ) and its transition point at low temperatures. *Nature*, Vol. 144, No. 3642, pp. 327–328, 1939.
- [12] Agus Subagyo and Kazuhisa Sueoka. Defect-induced charge freezing on epitaxial  $\text{Fe}_3\text{O}_4$  (001) film surfaces studied by spin-polarized scanning tunneling microscopy. *Japanese journal of applied physics*, Vol. 44, No. 7S, p. 5447, 2005.
- [13] A Subagyo and K Sueoka. Spin-polarized scanning tunneling microscopy study on charge ordering of reconstructed  $\text{Fe}_3\text{O}_4(001)$  film surfaces. *JAPANESE JOURNAL OF APPLIED PHYSICS PART 1-REGULAR PAPERS BRIEF COMMUNICATIONS & REVIEW PAPERS*, Vol. 45, No. 3B, pp. 2255–2258, MAR 2006.
- [14] W Eerenstein, TTM Palstra, T Hibma, and S Celotto. Origin of the increased resistivity in epitaxial  $\text{Fe}_3\text{O}_4$  films. *PHYSICAL REVIEW B*, Vol. 66, No. 20, NOV 15 2002.
- [15] W. Eerenstein, T. T. M. Palstra, S. S. Saxena, and T. Hibma. Spin-polarized transport across sharp antiferromagnetic boundaries. *Phys. Rev. Lett.*, Vol. 88, p. 247204, Jun 2002.
- [16] W. Eerenstein, T. T. M. Palstra, T. Hibma, and S. Celotto. Diffusive motion of antiphase domain boundaries in  $\text{Fe}_3\text{O}_4$  films. *Phys. Rev. B*, Vol. 68, p. 014428, Jul 2003.

- 
- [17] A. V. Ramos, J.-B. Moussy, M.-J. Guittet, A. M. Bataille, M. Gautier-Soyer, M. Viret, C. Gatel, P. Bayle-Guillemaud, and E. Snoeck. Magnetotransport properties of  $\text{Fe}_3\text{O}_4$  epitaxial thin films: Thickness effects driven by antiphase boundaries. *Journal of Applied Physics*, Vol. 100, No. 10, p. 103902, 2006.
- [18] D. T. Margulies, F. T. Parker, M. L. Rudee, F. E. Spada, J. N. Chapman, P. R. Aitchison, and A. E. Berkowitz. Origin of the anomalous magnetic behavior in single crystal  $\text{Fe}_3\text{O}_4$  films. *Phys. Rev. Lett.*, Vol. 79, pp. 5162–5165, Dec 1997.
- [19] G. Q. Gong, A. Gupta, Gang Xiao, W. Qian, and V. P. Dravid. Magnetoresistance and magnetic properties of epitaxial magnetite thin films. *Phys. Rev. B*, Vol. 56, pp. 5096–5099, Sep 1997.
- [20] A. Hamie, Y. Dumont, E. Popova, A. Fouchet, B. Warot-Fonrose, C. Gatel, E. Chikoidze, J. Scola, B. Berini, and N. Keller. Investigation of high quality magnetite thin films grown on  $\text{SrTiO}_3(001)$  substrates by pulsed laser deposition. *Thin Solid Films*, Vol. 525, No. 0, pp. 115 – 120, 2012.
- [21] F. C. Voogt, T. T. M. Palstra, L. Niesen, O. C. Rogojanu, M. A. James, and T. Hibma. Superparamagnetic behavior of structural domains in epitaxial ultrathin magnetite films. *Phys. Rev. B*, Vol. 57, pp. R8107–R8110, Apr 1998.
- [22] S. B. Ogale, K. Ghosh, R. P. Sharma, R. L. Greene, R. Ramesh, and T. Venkatesan. Magnetotransport anisotropy effects in epitaxial magnetite ( $\text{Fe}_3\text{O}_4$ ) thin films. *Phys. Rev. B*, Vol. 57, pp. 7823–7828, Apr 1998.
- [23] D. Reisinger, P. Majewski, M. Opel, L. Alff, and R. Gross. Hall effect, magnetization, and conductivity of  $\text{Fe}_3\text{O}_4$  epitaxial thin films. *Applied Physics Letters*, Vol. 85, No. 21, 2004.
- [24] D. T. Margulies, F. T. Parker, F. E. Spada, R. S. Goldman, J. Li, R. Sinclair, and A. E. Berkowitz. Anomalous moment and anisotropy behavior in  $\text{Fe}_3\text{O}_4$  films. *Phys. Rev. B*, Vol. 53, pp. 9175–9187, Apr 1996.

- [25] G. Hu and Y. Suzuki. Negative spin polarization of  $\text{Fe}_3\text{O}_4$  in magnetite/manganite-based junctions. *Phys. Rev. Lett.*, Vol. 89, p. 276601, Dec 2002.
- [26] W. Kim, K. Kawaguchi, N. Koshizaki, M. Sohma, and T. Matsumoto. Fabrication and magnetoresistance of tunnel junctions using half-metallic  $\text{Fe}_3\text{O}_4$ . *J. Appl. Phys.*, Vol. 93, No. 10, pp. 8032–8034, 2003.
- [27] Keith P McKenna, Florian Hofer, Daniel Gilks, Vlado K Lazarov, Chunlin Chen, Zhongchang Wang, and Yuichi Ikuhara. Atomic-scale structure and properties of highly stable antiphase boundary defects in  $\text{Fe}_3\text{O}_4$ . *Nature communications*, Vol. 5, , 2014.
- [28] A. Pratt, M. Kurahashi, X. Sun, D. Gilks, and Y. Yamauchi. Direct observation of a positive spin polarization at the (111) surface of magnetite. *Phys. Rev. B*, Vol. 85, p. 180409, May 2012.
- [29] Y.J. Kim, Y. Gao, and S.A. Chambers. Selective growth and characterization of pure, epitaxial  $\alpha$ - $\text{Fe}_2\text{O}_3(0001)$  and  $\text{Fe}_3\text{O}_4(001)$  films by plasma-assisted molecular beam epitaxy. *Surface Science*, Vol. 371, No. 23, pp. 358 – 370, 1997.
- [30] S.A Chambers and S.A Joyce. Surface termination, composition and reconstruction of  $\text{Fe}_3\text{O}_4(001)$  and  $\gamma$ - $\text{Fe}_2\text{O}_3(001)$ . *Surface Science*, Vol. 420, No. 23, pp. 111 – 122, 1999.
- [31] SA Chambers, S Thevuthasan, and SA Joyce. Surface structure of MBE-grown  $\text{Fe}_3\text{O}_4(001)$  by X-ray photoelectron diffraction and scanning tunneling microscopy. *SURFACE SCIENCE*, Vol. 450, No. 1-2, pp. L273–L279, APR 1 2000.
- [32] B Stanka, W Hebenstreit, U Diebold, and SA Chambers. Surface reconstruction of  $\text{Fe}_3\text{O}_4(001)$ . *SURFACE SCIENCE*, Vol. 448, No. 1, pp. 49–63, MAR 1 2000.

- 
- [33] R. Bliem, E. McDermott, P. Ferstl, M. Setvin, O. Gamba, J. Pavelec, M. A. Schneider, M. Schmid, U. Diebold, P. Blaha, L. Hammer, and G. S. Parkinson. Subsurface cation vacancy stabilization of the magnetite (001) surface. *Science*, Vol. 346, No. 6214, pp. 1215–1218, 2014.
- [34] IV Shvets, G Mariotto, K Jordan, N Berdunov, R Kantor, and S Murphy. Long-range charge order on the Fe<sub>3</sub>O<sub>4</sub>(001) surface. *PHYSICAL REVIEW B*, Vol. 70, No. 15, OCT 2004.
- [35] M. Fonin, Yu S. Dedkov, R. Pentcheva, U. Ruediger, and G. Guentherodt. Spin-resolved photoelectron spectroscopy of Fe(3)O(4)-revisited. *JOURNAL OF PHYSICS-CONDENSED MATTER*, Vol. 20, No. 14, APR 9 2008.
- [36] G Mariotto, S Murphy, and IV Shvets. Charge ordering on the surface of Fe<sub>3</sub>O<sub>4</sub>(001). *PHYSICAL REVIEW B*, Vol. 66, No. 24, DEC 15 2002.
- [37] A. Subagy, Y. Sasaki, H. Oka, and K. Sueoka. Inhomogeneous surface electronic properties and charge ordering in epitaxial Fe<sub>3</sub>O<sub>4</sub> films On MgO(001). *PHYSICA STATUS SOLIDI B-BASIC SOLID STATE PHYSICS*, Vol. 244, No. 12, pp. 4482–4485, DEC 2007. International Symposium on Advanced Magnetic Materials and Applications, Cheju Isl, SOUTH KOREA, MAY 28-JUN 01, 2007.
- [38] Zbynek Novotny, Narasimham Mulakaluri, Zoltan Edes, Michael Schmid, Rossitza Pentcheva, Ulrike Diebold, and Gareth S. Parkinson. Probing the surface phase diagram of fe<sub>3</sub>o<sub>4</sub>(001) towards the fe-rich limit: Evidence for progressive reduction of the surface. *Phys. Rev. B*, Vol. 87, p. 195410, May 2013.
- [39] Zbyněk Novotný, Giacomo Argentero, Zhiming Wang, Michael Schmid, Ulrike Diebold, and Gareth S. Parkinson. Ordered array of single adatoms with remarkable thermal stability: Au/fe<sub>3</sub>o<sub>4</sub>(001). *Phys. Rev. Lett.*, Vol. 108, p. 216103, May 2012.

- 
- [40] Akira Ikeuchi, Satoshi Hiura, Taichi Mizuno, Eisaku Kaji, Agus Subagyo, and Kazuhisa Sueoka. Atomically resolved observations of antiphase domain boundaries in epitaxial  $\text{Fe}_3\text{O}_4$  films on  $\text{MgO}$  (001) by scanning tunneling microscopy. *Japanese Journal of Applied Physics*, Vol. 51, No. 8S3, p. 08KB02, 2012.
- [41] J. A. Stroscio, R. M. Feenstra, and A. P. Fein. “Electronic structure of the Si(111)  $2 \times 1$  surface by scanning tunneling microscopy”. *Phys. Rev. Lett.*, Vol. **57**, pp. 2579–2582, (1986).
- [42] R. M. Feenstra, J. A. Stroscio, and A. P. Fein. “Tunneling spectroscopy of the Si(111)  $2 \times 1$  surface”. *Surf. Sci.*, Vol. **181**, pp. 295–306, (1987).
- [43] T. Balashov, A. F. Takacs, W. Wulfhekel, and J. Kirschner. “Magnon Excitation with Spin-Polarized Scanning Tunneling Microscopy”. *Phys. Rev. Lett.*, Vol. **97**, p. 187201, (2006).
- [44] G. Binnig, H. Rohrer, C. Gerber, and E. Weibel. “Spin-polarized electron microscopy”. *Helv. Phys. Acta*, Vol. **55**, p. 726, (1982).
- [45] J. A. Stroscio, R. M. Feenstra, and A. P. Fein. “Local state density and long-range screening of adsorbed oxygen atoms on the GaAs(110) surface”. *Phys. Rev. Lett.*, Vol. **58**, pp. 1668–1671, (1987).
- [46] P. Mårtensson and R. M. Feenstra. “Geometric and electronic structure of antimony on the GaAs(110) surface studied by scanning tunneling microscopy”. *Phys. Rev. B*, Vol. **39**, pp. 7744–7753, (1989).
- [47] R. Wiesendanger, H. J. Güntherodt, G. Güntherodt, G. J. Gambion, and R. Ruf. “Observation of vacuum tunneling of spin-polarized electrons with the scanning tunneling microscope”. *Phys. Rev. Lett.*, Vol. **65**, pp. 247–250, 1990.
- [48] R. Wiesendanger, I. V. Shvets, D. Bürgler, G. Tarrch, H. J. Güntherodt, J. M. D. Coey, and S. Gräser. “Topographic and Magnetic-Sensitive Scanning

- Tunneling Microscope Study of Magnetite”. *Science*, Vol. **255**, pp. 583–586, 1992.
- [49] M. Bode, M. Getzlaff, and R. Wiesendanger. “Spin-Polarized Vacuum Tunneling into the Exchange-Split Surface State of Gd(0001)”. *Phys. Rev. Lett.*, Vol. **81**, pp. 4256–4259, 1998.
- [50] M. Bode, M. Getzlaff, and R. Wiesendanger. “Quantitative aspects of spin-polarized scanning tunneling spectroscopy of Gd(0001)”. *J. Vac. Sci. Technol. A*, Vol. **17**, pp. 2228–2232, 1999.
- [51] G. Binnig and H. Rohrer. “Scanning tunnelling microscopy”. *Helv. Phys. Acta*, Vol. **55**, pp. 726–735, (1982).
- [52] G. Binnig, H. Rohrer, C. Gerber, and E. Weibel. “7 x 7 Reconstruction on Si(111) Resolved in Real Space”. *Phys. Rev. Lett.*, Vol. **50**, pp. 120–123, (1982).
- [53] J. Bardeen. “Tunnelling from a Many-Particle Point of View”. *Phys. Rev. Lett.*, Vol. **6**, pp. 57–59, (1961).
- [54] N. Garcia, C. Ocal, and F. Flores. “Model Theory for Scanning Tunneling Microscopy: Application to Au(110)(1 × 2)”. *Phys. Rev. Lett.*, Vol. **50**, pp. 2002–2005, (1983).
- [55] N. D. Lang. “Theory of single-atom imaging in the scanning tunneling microscope”. *Phys. Rev. Lett.*, Vol. **56**, pp. 1164–1167, (1986).
- [56] C. J. Chen. “Introduction to Scanning Tunneling Microscopy”. Oxford University Press, (1993).
- [57] U. Schlickum, N. Janke-Gilman, W. Wulfhekel, and J. Kirschner. “Step-Induced Frustration of Antiferromagnetic Order in Mn on Fe(001)”. *Phys. Rev. Lett.*, Vol. **92**, p. 107203, (2004).

- 
- [58] U. Schlickum, W. Wulfhekel, and J. Kirschner. “Spin-polarized scanning tunneling microscope for imaging the in-plane magnetization”. *Appl. Phys. Lett.*, Vol. **83**, pp. 2016–2018, (2003).
- [59] T. K. Yamada, M. M. J. Bischoff, T. Mizoguchi, and H. van Kempen. “STM and STS study of ultrathin Mn layers on Fe(001)”. *Surf. Sci.*, Vol. **501**, pp. 179–190, 2002.
- [60] T. K. Yamada, M. M. J. Bischoff, G. M. M. Heijnen, T. Mizoguchi, and H. V. Kempen. “Observation of Spin-Polarized Surface States on Ultrathin bct Mn(001) Films by Spin-Polarized Scanning Tunneling Spectroscopy”. *Phys. Rev. Lett.*, Vol. **90**, pp. 56803–1–4, 2003.
- [61] T. K. Yamada, M. M. J. Bischoff, T. Mizoguchi, and H. van Kempen. “Use of voltage pulses to detect spin-polarized tunneling”. *Appl. Phys. Lett.*, Vol. **82**, pp. 1437–1439, 2003.
- [62] T. K. Yamada, M. M. J. Bischoff, G. M. M. Heijnen, T. Mizoguchi, and H. van Kempen. “Origin of Magnetic Contrast in Spin-Polarized Scanning Tunneling Spectroscopy: Experiments on Ultra-Thin Mn Films”. *Jpn. J. Appl. Phys.*, Vol. **42**, pp. 4688–4691, 2003.
- [63] T. Matsuda, A. Tonomura, T.K. Yamada, D. Okuyama, N. Mizuno, A.L. Vazquez de Parga, H. van Kempen, and T.Mizoguchi. “Characterization of Fe/W spin-polarized tips by means of holographic TEM and spin-polarized STS of optically pumped p-GaAs”. *IEEE Transactions and Magnetism (the 2005 InterMAG conference)*, Vol. **41**, pp. 3727–3729, 2005.
- [64] T. Kawagoe, Y. Iguchi, T. Miyamachi, A. Yamasaki, and S. Suga. “Spiral Terraces and Spin Frustration in Layered Antiferromagnetic Cr (001) Films”. *Phys. Rev. Lett.*, Vol. **95**, p. 207205, 2004.

- 
- [65] J. Prokop, A. Kukunin, and H. J. Elmers. “Spin-polarized scanning tunneling microscopy and spectroscopy of ultrathin Fe/Mo(110) films using W/Au/Co tips”. *Phys. Rev. B*, Vol. **73**, p. 014428, 2006.
- [66] K. Sueoka, K. Mukasa, and K. Hayakawa. “Possibility of observing spin-polarized tunneling current using scanning tunneling microscopy with optically pumped GaAs”. *Jpn. J. Appl. Phys.*, Vol. **32**, pp. 2989–2993, 1993.
- [67] D. T. Pierce. “Spin-polarized electron microscopy”. *Phys. Scr.*, Vol. **38**, pp. 291–296, (1988).
- [68] R. Shinohara, K. Yamaguchi, Y. Suzuki, and W. Nabhan. “Fabrication of GaAs Microtips and Their Application to Spin-Polarized Scanning Tunneling Microscope”. *Jpn. J. Appl. Phys.*, Vol. **37**, pp. 7151–7154, 1998.
- [69] R. Shinohara, K. Yamaguchi, H. Hirota, Y. Suzuki, T. Manago, H. Akinaga, and T. Kuroda and F. Minami. “Lifetime and Spin Relaxation Time Measurements of Micro-Fabricated GaAs Tips”. *Jpn. J. Appl. Phys.*, Vol. **39**, pp. 7093–7096, 2000.
- [70] M. Kleiber, M. Bode, R. Ravlić, and R. Wiesendanger. Topology-induced spin frustrations at the cr(001) surface studied by spin-polarized scanning tunneling spectroscopy. *Phys. Rev. Lett.*, Vol. 85, p. 4606, 2000.
- [71] A. Kubetzka, O. Pietzsch, M. Bode, and R. Wiesendanger. “Magnetism of nanoscale Fe islands studies by spin-polarized scanning tunneling spectroscopy”. *Phys. Rev. B*, Vol. **63**, pp. 140407–1–4, 2001.
- [72] A. Kubetzka, P. Ferriani, M. Bode, S. Heinze, G. Bihlmayer, K. von Bergmann, O. Pietzsch, S. Blügel, and R. Wiesendanger. “Revealing Antiferromagnetic Order of the Fe Monolayer on W(001): Spin-Polarized Scanning Tunneling Microscopy and First-Principles Calculations”. *Phys. Rev. Lett.*, Vol. **94**, p. 187204, 2005.

- 
- [73] S. Blügel, D. Pescia, and P. Dederichs. Ferromagnetism versus antiferromagnetism of the  $\text{cr}(001)$  surface. *Phys. Rev. B*, Vol. 39, pp. 1392–1394, Jan 1989.
- [74] M. Kleiber, M. Bode, R. Ravlić, and R. Wiesendanger. Topology-induced spin frustrations at the  $\text{cr}(001)$  surface studied by spin-polarized scanning tunneling spectroscopy. *Phys. Rev. Lett.*, Vol. 85, pp. 4606–4609, Nov 2000.
- [75] Ze Zhang and Sashi Satpathy. Electron states, magnetism, and the verwey transition in magnetite. *Phys. Rev. B*, Vol. 44, pp. 13319–13331, Dec 1991.
- [76] T Hibma, FC Voogt, L Niesen, PAA van der Heijden, WJM de Jonge, JJTM Donkers, and PJ van der Zaag. Anti-phase domains and magnetism in epitaxial magnetite layers. *JOURNAL OF APPLIED PHYSICS*, Vol. 85, No. 8, Part 2B, pp. 5291–5293, APR 15 1999.
- [77] S Celotto, W Eerenstein, and T Hibma. Characterization of anti-phase boundaries in epitaxial magnetite films. *EUROPEAN PHYSICAL JOURNAL B*, Vol. 36, No. 2, pp. 271–279, NOV 2003.
- [78] D. T. Margulies, F. T. Parker, M. L. Rudee, F. E. Spada, J. N. Chapman, P. R. Aitchison, and A. E. Berkowitz. Origin of the anomalous magnetic behavior in single crystal  $\text{Fe}_3\text{O}_4$  films. *Phys. Rev. Lett.*, Vol. 79, pp. 5162–5165, Dec 1997.
- [79] R. G. S. Sofin, S. K. Arora, and I. V. Shvets. Positive antiphase boundary domain wall magnetoresistance in  $\text{Fe}_3\text{O}_4$  (110) heteroepitaxial films. *Phys. Rev. B*, Vol. 83, p. 134436, Apr 2011.
- [80] M Fonin, R Pentcheva, YS Dedkov, M Sperlich, DV Vyalikh, M Scheffler, U Rudiger, and G Guntherodt. Surface electronic structure of the  $\text{Fe}_3\text{O}_4(100)$ : Evidence of a half-metal to metal transition. *PHYSICAL REVIEW B*, Vol. 72, No. 10, SEP 2005.
- [81] FC Voogt, T Fujii, PJM Smulders, L Niesen, MA James, and T Hibma.  $\text{NO}_2$ -assisted molecular-beam epitaxy of  $\text{Fe}_3\text{O}_4$ ,  $\text{Fe}_3\text{-delta O}_4$ , and  $\gamma\text{-Fe}_2\text{O}_3$

- thin films on MgO(100). *PHYSICAL REVIEW B*, Vol. 60, No. 15, pp. 11193–11206, OCT 15 1999.
- [82] PG Bercoff and HR Bertorello. Exchange constants and transfer integrals of spinel ferrites. *JOURNAL OF MAGNETISM AND MAGNETIC MATERIALS*, Vol. 169, No. 3, pp. 314–322, MAY 1997.
- [83] C. M. Srivastava, G. Srinivasan, and N. G. Nanadikar. Exchange constants in spinel ferrites. *Phys. Rev. B*, Vol. 19, pp. 499–508, Jan 1979.
- [84] Nobuyuki Ishida, Agus Subagyo, Akira Ikeuchi, and Kazuhisa Sueoka. Holders for in situ treatments of scanning tunneling microscopy tips. *Review of Scientific Instruments*, Vol. 80, No. 9, pp. –, 2009.
- [85] Gareth S. Parkinson, Thomas A. Manz, Zbyněk Novotný, Phillip T. Sprunger, Richard L. Kurtz, Michael Schmid, David S. Sholl, and Ulrike Diebold. Antiphase domain boundaries at the  $\text{Fe}_3\text{O}_4(001)$  surface. *Phys. Rev. B*, Vol. 85, p. 195450, May 2012.
- [86] R WIESENDANGER, IV SHVETS, D BURGLER, G TARRACH, HJ GUNTHERODT, JMD COEY, and S GRASER. TOPOGRAPHIC AND MAGNETIC-SENSITIVE SCANNING TUNNELING MICROSCOPE STUDY OF MAGNETITE. *SCIENCE*, Vol. 255, No. 5044, pp. 583–586, JAN 31 1992.
- [87] JMD COEY, IV SHVETS, R WIESENDANGER, and HJ GUNTHERODT. CHARGE FREEZING AND SURFACE ANISOTROPY ON MAGNETITE(100). *JOURNAL OF APPLIED PHYSICS*, Vol. 73, No. 10, Part 2b, pp. 6742–6744, MAY 15 1993. 37TH ANNUAL CONF ON MAGNETISM AND MAGNETIC MATERIALS, HOUSTON, TX, DEC 01-04, 1992.
- [88] R Koltun, M Herrmann, G Guntherodt, and VAM Brabers. Enhanced atomic-scale contrast on  $\text{Fe}_3\text{O}_4(100)$  observed with an FeSTM tip. *APPLIED*

*PHYSICS A-MATERIALS SCIENCE & PROCESSING*, Vol. 73, No. 1, pp. 49–53, JUL 2001.

- [89] K. Jordan, A. Cazacu, G. Manai, S. F. Ceballos, S. Murphy, and I. V. Shvets. Scanning tunneling spectroscopy study of the electronic structure of Fe<sub>3</sub>O<sub>4</sub> surfaces. *PHYSICAL REVIEW B*, Vol. 74, No. 8, AUG 2006.

# Publication List

- (1) A. Ikeuchi, S. Hiura, T. Mizuno, E. Kaji, A. Subagyo and K. Sueoka. “Atomically Resolved Observations of Antiphase Domain Boundaries in Epitaxial  $\text{Fe}_3\text{O}_4$  Films on  $\text{MgO}(001)$  by Scanning Tunneling Microscopy”. *Japanese Journal of Applied Physics* Vol. 51, 08KB02, 2012.

# International Conference

- (1) A. Ikeuchi, A. Subagyo, E. Kaji and K. Sueoka. “STM/STS Study of Structural Properties of Antiphase Domain Boundaries in Epitaxial  $\text{Fe}_3\text{O}_4$  Films on  $\text{MgO}(100)$ ”. International Scanning Probe Microscopy Conference (ISPM 2011), p.74, P02, Munich, June 2011.
- (2) A. Ikeuchi, A. Subagyo, S. Hiura and K. Sueoka. “Structural and Electronic Properties around Antiphase Domain Boundaries in Epitaxial  $\text{Fe}_3\text{O}_4$  Films on  $\text{MgO}(100)$ ”. The 19th International Colloquium on Scanning Probe Microscopy (ICSPM19), p.109, S4-72, Toyako-cho, December 2011.
- (3) A. Ikeuchi, S. Hiura, A. Subagyo and K. Sueoka. “Surface Atomic Configurations and Electronic properties around Antiphase Domain Boundaries in  $\text{Fe}_3\text{O}_4/\text{MgO}(001)$ ”. International Conference on Nanoscience + Nanotechnology (ICN+T 2012), p.174, PO6.15, Paris, France, July 2012.
- (4) A. Ikeuchi, A. Subagyo, S. Hiura and K. Sueoka. “Surface Electronic Properties in Anti-phase Domain on Epitaxially grown  $\text{Fe}_3\text{O}_4/\text{MgO}(100)$ ”. The 20th International Colloquium on Scanning Probe Microscopy (ICSPM20), p.109, S4-72, Naha, December 2012.
- (5) A. Ikeuchi, S. Hiura, A. Subagyo and K. Sueoka. “Surface Electronic Properties on Magnetite Films on  $\text{MgO}(100)$ ”. International Conference on Nanoscience + Technology (ICN+T 2013), p.83, SS-P1-16, Paris, September 2013.
- (6) A. Ikeuchi, S. Hiura, S. Shirini, A. Subagyo and K. Sueoka. “Surface Electronic Properties of Anti-phase Domain in  $\text{Fe}_3\text{O}_4(001)$  Thin Films”. The 21th International Colloquium on Scanning Probe Microscopy (ICSPM21), p.250, 8PN-87, Tsukuba, November 2013.